

The Effects of Surface Heterogeneity Scale on the Flux Imbalance under Free Convection

Yanzhao Zhou^{1, 2, 3}, Dan Li⁴, and Xin Li^{1, 5}

¹Institute of Tibetan Plateau Research, Chinese Academy of Sciences, Beijing, 100101, China.

²Key Laboratory of Remote Sensing of Gansu Province, Northwest Institute of Eco-Environment and Resources, Chinese Academy of Sciences, Lanzhou, 730000, Gansu, China.

³University of Chinese Academy of Sciences, Beijing, 100101, China.

⁴Department of Earth and Environment, Boston University, Boston, 02215, Massachusetts, USA.

⁵CAS Center for Excellence in Tibetan Plateau Earth Sciences, Chinese Academy of Sciences, Beijing, 100101, China.

Corresponding author: Xin Li (xinli@itpcas.ac.cn) and Dan Li (lidan@bu.edu)

Key Points:

- The flux imbalance (I) is controlled by the z_i/L , l_w , U , and T .
- A diagnostic equation for the flux imbalance is proposed as $I = 1 - [az/z_i + b][-K \times z_i/L \times l_w/UT + C]$, where a , b , K , and C are empirical constants.
- The qualitative relations between the flux imbalance and various factors reported in the literature can be explained by this model.

Abstract It is well known that the available energy (i.e., the net radiation minus the ground heat flux) is often 10% - 30% larger than the sum of turbulent fluxes measured by the eddy-covariance method. Although field observations and previous large-eddy simulation (LES) studies have shown that surface heterogeneity can induce flux imbalance, the relationship between the flux imbalance magnitude and surface heterogeneity scale remains to be investigated in more detail. Here, we examine the flux imbalance over landscapes characterized by different surface heterogeneity scales in a dry freely convective boundary layer. We reveal that the flux imbalance initially increases with increasing surface heterogeneity scale. However, when the surface heterogeneity scale becomes larger than the boundary-layer height, the surface starts to behave locally homogeneous, which leads to a lower flux imbalance. Based on LES results, we propose a conceptual model to explain how the domain average flux imbalance is influenced by surface heterogeneity. The flux imbalance is found to be controlled by the ratio of boundary-layer height to the Obukhov length ($-z_i/L$), the integral length scale of vertical velocity (l_w), the mean horizontal speed (U), and the time averaging interval (T). Among these four variables, l_w determines the size of turbulent coherent structures (i.e., large eddies); whereas $-z_i/L$ affects the form of these large eddies. Meanwhile, the U and T determine how many these large eddies can be sampled by the eddy-covariance. This finding indicates that it may be possible to diagnose the flux imbalance using these four variables under convective conditions.

Keywords Convective boundary layer • Flux imbalance • Large eddy simulation • Surface heterogeneity scale

1 Introduction

The eddy-covariance (EC) method is one of the most common methods for measuring turbulent exchanges between the biosphere and the atmosphere. The fluxes of heat, water vapor and CO₂ measured at EC sites around the world (e.g., FLUXNET, Baldocchi et al., 2001) are widely used for developing and validating land surface schemes (Williams et al., 2009; Li et al., 2013, 2016, 2017), and for climatological studies (Jung et al., 2010). However, a **long-standing problem with the EC method** is observed in which, the sum of the sensible and latent heat fluxes by EC is smaller than the difference between the net radiation and ground heat flux (Aubinet et al., 2012; Foken, 2008; Leuning et al. 2012; Oncley et al., 2007; Twine et al., 2000; Wilson et al., 2002; Xu et al., 2017). This systematic bias in the EC method, which is more pronounced over heterogeneous surfaces than homogeneous surfaces, is called the surface energy imbalance or non-closure problem and is one of the biggest challenges for the EC measurement technique.

Potential reasons for this energy imbalance include mismatch in the footprints of radiation and turbulent flux measurements, measurement or computation errors, significant advective fluxes, and inadequate sampling of large-scale, low-frequency turbulent eddies, as reviewed elsewhere (Mahrt, 1998; Twine et al., 2000; Foken et al, 2006; Foken, 2008; Wang et al., 2009; Foken et al., 2011; Leuning et al. 2012; Wohlfahrt and Widmoser, 2013; Zhou and Li, 2018). Among these potential causes, the inadequate sampling of large-scale turbulent eddies has been increasingly acknowledged as one of the leading contributors to the surface energy imbalance (Foken et al., 2011).

Over homogeneous terrain, the largest turbulent eddy scales with the boundary-layer height (Wyngaard, 1985; Stull, 1988). Over heterogeneous terrain, secondary circulations can be further induced by the landscape-level heterogeneity around EC sites (Foken et al, 2006). These large-scale turbulent eddies and secondary circulations may not be adequately sampled by an EC

tower in a finite averaging period (e.g., 30 mins); hence, an imbalance occurs. This phenomenon has been confirmed by many observational (Panin et al., 1998; Stoy et al., 2013; Eder et al., 2015a; Gao et al., 2017; Xu et al., 2017) and large-eddy simulation (LES) studies (Kanda et al., 2004; Inagaki et al., 2006; Steinfeld et al., 2007; Huang et al., 2008; Eder et al., 2015b; Schalkwijk et al., 2016; De Roo and Mauder, 2018; Zhou et al., 2018).

Over the past decade, our understanding of the flux imbalance has been significantly advanced and many factors were found to be related to the flux imbalance (see Table 1). However, it remains elusive as to (i) how the flux imbalance is influenced by surface heterogeneity and (ii) what the relationship between the flux imbalance and the surface heterogeneity scale is. For example, although previous studies have shown that surface heterogeneity is a major factor causing flux imbalance (Zhou et al., 2018) and various energy balance closure parametrization schemes have been proposed (Panin et al., 1998; Huang et al., 2008; Panin and Bernhofer, 2008), the key flow parameters and surface variables controlling the flux imbalance magnitude remain debated (Eder et al., 2014). In addition, while field observations (Stoy et al., 2013; Xu et al., 2017) have shown that the flux imbalance magnitude generally increases as the surface heterogeneity becomes stronger, large variations occur in such relations. Addressing these two questions frames the scope of our study.

The paper is structured as follows: Section 2 describes the method; Section 3 provides details on the LES model and the numerical experiments. The results are described in Section 4 and discussed in Section 5. Finally, Section 6 concludes the paper.

2 Method

2.1 Flux imbalance over heterogeneous surfaces

We consider a variable φ with the horizontal spatial mean as $[\varphi](z, t)$ and the temporal mean as $\overline{\varphi}(x, y, z)$. Fluctuations from the spatial and temporal means are denoted as φ'' and φ' , respectively. The general definition of flux imbalance magnitude (I) is the difference between “true flux” and the turbulent flux, which can be expressed as follows:

$$I = \frac{TF - TU}{TF}, \quad (1)$$

where TU denotes the turbulent flux (e.g., measured by the EC) and TF represents the “true flux”. Note that here I represents the flux imbalance magnitude as TU is often smaller than TF . This is slightly different from the flux imbalance defined in previous studies (Kanda et al., 2004; Inagaki et al., 2006; Steinfeld et al., 2007; Huang et al., 2008; Schalkwijk et al., 2016; Zhou et al., 2018), which is often $(-I)$.

Finnigan et al. (2003) used a control volume approach to discuss the assumptions and limitations of the EC method. In their method, the surface heat flux (HFX) is treated as the “true flux”. Following their method, the domain averaged flux imbalance can thus be calculated as follows:

$$[I] = \frac{[HFX] - [\overline{w'\theta'}]}{[HFX]}, \quad (2)$$

where $[I]$ represents the difference between the mean turbulent flux and mean true flux.

It should be pointed out that in some previous studies (Kanda et al., 2004; Inagaki et al., 2006; Steinfeld et al., 2007; Huang et al., 2008; Schalkwijk et al., 2016; Zhou et al., 2018), the spatiotemporally averaged vertical heat flux ($\overline{w\theta}$) at a given height is used as the “true flux”. This method is often used over homogeneous surfaces (e.g., Kanda et al., 2004; Steinfeld et al., 2007; Huang et al., 2008; Schalkwijk et al., 2016; Zhou et al., 2018) and 1-D heterogeneous surfaces (Inagaki et al., 2006; Zhou et al., 2018). The use of spatiotemporally averaged vertical heat flux ($\overline{w\theta}$) as the true flux over heterogeneous surfaces is complicated by the existence of mean vertical motions (Zhou et al. 2018). Hence, in this study, we use the surface flux as the true flux.

2.2 The surface heterogeneity scale

Many previous LES studies focused on idealized heterogeneity, such as striped-like and chessboard-like heterogeneities with uniform sizes (Chen and Avissar, 1994; Avissar and Schmidt, 1998). For these idealized heterogeneity patterns, the characteristic length scale can be relatively easily defined. For example, the width of the strip can be used to indicate the length scale of surface heterogeneity. Recently, more complex and/or realistic landscape patterns based on remote sensing have been used (Albertson et al., 2001; Kustas and Albertson, 2003; Bertoldi et al., 2007; Huang and Margulis, 2009; Liu et al., 2017). To characterize the length scale of surface heterogeneity (L_p) over complex landscape patterns, Bou-Zeid et al., (2007) (hereafter B07) proposed to define L_p as follows:

$$L_p = \int_0^{L_D} \left[1 - \frac{D(r)}{\max(D)} \right] dr, \quad (3)$$

where L_D is the streamwise length of the domain and $D(r)$ is the structure function of the analyzed surface characteristics (e.g., momentum roughness length) with distance r along the streamwise direction. On the other hand, Huang and Margulis (2009) (hereafter HM09) used a normalized exponential variogram model to define the characteristic length scale:

$$L_p = -\frac{\ln \gamma}{3d}, \quad (4)$$

where the d is the distance matrix representing the distance between any two points and γ is the variogram. The details about the two methods can be found in B07 and HM09.

2.3 A conceptual model based on the cospectral shape

As stated in the introduction, the flux imbalance is assumed to be mainly caused by the large eddies. Under this assumption, it is more convenient and easier to interpret the flux imbalance from the cospectral point view. To do so, we employ the cospectrum of w and θ , which describes the distribution of vertical potential temperature flux among scales. Nonetheless, it should be stressed that our aim is not to propose a cospectral model to calculate the flux imbalance directly, but rather to develop a conceptual model based on the cospectral shape to better understand the flux imbalance and explore the flow and surface variables that affect the flux imbalance.

Figure 1a presents a schematic illustrating the cospectrum of heat flux ($F_{w\theta}$), where k is the wavenumber and k_p is the wavenumber at which $F_{w\theta}$ reaches its peak (hereafter the peak wavenumber). Based on the assumption that the large eddies are responsible for the flux

imbalance, we assume that the EC method can only sample eddies that are larger (smaller) than a critical wavenumber (wavelength), which is referred to as k_{ec} (Fig. 1a). The above assumption also implicitly employs Taylor's hypothesis which converts temporal measurements at a point (e.g., the EC measurements) to spatial information, i.e., from frequency (f) to wavenumber (k), retaining the shape and magnitude of spectra (Kaimal and Finnigan, 1994). Therefore, the flux imbalance or Eq. (2) can be calculated as follows:

$$\begin{aligned}
 [I] &= 1 - \frac{[\overline{w'\theta'}]}{[HFX]} = 1 - \frac{\int_{k_{ec}}^{\infty} F_{w\theta}(k, z) dk}{[HFX]} \\
 &= 1 - \frac{\int_0^{\infty} F_{w\theta}(k, z) dk \left(1 - \frac{\int_0^{k_{ec}} F_{w\theta}(k, z) dk}{\int_0^{\infty} F_{w\theta}(k, z) dk} \right)}{[HFX]}.
 \end{aligned} \tag{5}$$

The above expression can be reformulated as Eq. (6), with Eq. (7) and Eq. (8) as follows,

$$[I] = 1 - f_1 f_2. \tag{6}$$

$$f_1 = \frac{\int_0^{\infty} F_{w\theta}(k, z) dk}{[HFX]}. \tag{7}$$

$$f_2 = 1 - \frac{\int_0^{k_{ec}} F_{w\theta}(k, z) dk}{\int_0^{\infty} F_{w\theta}(k, z) dk} = \frac{1 - [I]}{f_1}. \tag{8}$$

In Eq. (6), f_1 is the ratio of the “flux at height z ” to the surface flux, which represents the reduction of flux as z increases. The term f_2 represents the role of large eddies in causing flux imbalance at height z . From Eq. (6) it can be seen that the flux imbalance magnitude increases with decreasing f_1 and decreasing f_2 .

To further understand the behaviors of f_1 and f_2 , we turn to the cospectrum. Different functional forms have been used for the cospectrum $F_{w\theta}$ (Kaimal and Finnigan, 1994; Massman and Lee, 2002; Lee et al., 2005; Katul et al., 2013). In this paper, we use the model of Massman and Clement (2005) for illustration purpose, as follows:

$$F_{w\theta}(k) = \frac{A}{k_p \left[1 + m \left(\frac{k}{k_p} \right)^{2\mu} \right]^{\frac{1}{2\mu} \times \frac{m+1}{m}}}, \tag{9}$$

where A is a normalization parameter, m and μ are the (inertial subrange) slope parameter and broadness parameter, respectively. When $m = 3/4$, Eq. (9) reproduces the $-7/3$ power law of $F_{w\theta}$ in the inertial subrange (Lumley, 1967; Li and Katul, 2017). When $\mu = 0.5$, Eq. (9) reproduces the observed cospectrum from the famous Kansas experiment (Kaimal et al., 1976), which is commonly used as the standard in the cospectral correction of EC observations (Moore, 1986). Substituting Eq. (9) into Eq. (5), the f_2 term can be expressed as:

$$f_2 = \frac{\Gamma\left(\frac{1}{2\mu}, \frac{m+1}{2\mu} \left(\frac{k_{ec}}{k_p}\right)^{2\mu}\right)}{\Gamma\left(\frac{1}{2\mu}, 0\right)}, \quad (10)$$

where Γ is the **incomplete Gamma function**. The detailed derivation of Eq. (10) is presented in Appendix A. Because m and μ are positive and $\Gamma(s, x)$ decreases with increasing x , Eq. (10) indicates that f_2 decreases with increasing k_{ec}/k_p . Similar results as Eq. (10) can be obtained using other cospectral models as shown in Appendix B but the relation between f_2 and k_{ec}/k_p strongly depends on the assumed cospectral model. It should be pointed out that these cospectrum models are derived from homogeneous surfaces; over heterogeneous surfaces, their shapes, especially in the range of low wavenumbers, are likely to be different from those over homogeneous surfaces. As such, we will not use the exact relation between f_2 and k_{ec}/k_p given by the Massman and Clement (2005) model (namely, Eq. 10) in our calculation. Instead, the Eq. (10) is meant to provide a qualitative description of the relation between f_2 and k_{ec}/k_p (i.e., f_2 is expected to decrease with increasing k_{ec}/k_p). In Sect. 4.2 we will compute f_1 from Eq. (7) assuming that $\int_0^\infty F_{w\theta}(k, z) dk = [w''\theta'']$ and hence $f_1 = [w''\theta'']/[HFX]$, and then explore the relation between f_2 , which will be inferred as $(1-[I])/f_1$ (see Eq. 8), and k_{ec}/k_p .

Now we detail how k_{ec}/k_p is estimated (or approximated). Based on sampling theory, the larger the eddy moving velocity (say, represented by u), the more eddies can be sampled by the EC in a finite averaging period (T) and hence the smaller the flux imbalance. Therefore, k_{ec} may be represented by $1/(uT)$. A reasonable estimate for u is the horizontal mean wind speed U by invoking Taylor's hypothesis, which assumes that turbulent eddies are simply advected by the mean flow when they pass a fixed point. Note that the horizontal mean "velocity" under free convective conditions should be equal to 0 but here we use the horizontal mean wind "speed", which is calculated locally as $\sqrt{U_x^2 + U_y^2}$ and then averaged over the domain. To distinguish it from the horizontal mean velocity, we call it "the mean wind speed U ". However, given the limitation of Taylor's hypothesis in constructing very large-scale structures in turbulent boundary layers (Dennis and Nickels, 2008), we will also examine other velocity scales such as the convective velocity w_* , which is defined as follows:

$$w_* = \left(\frac{g}{\rho} z_i \frac{H}{c_p \theta_0}\right)^{\frac{1}{3}}, \quad (11)$$

where g is the gravitational acceleration, θ_0 is the reference potential temperature, c_p is the specific heat of air, and z_i is the boundary-layer height. In addition, we will consider the friction velocity $u_* = \sqrt{\tau/\rho}$, where τ is the surface drag and ρ is the air density, as well as the square root of turbulent kinetic energy (TKE) ($\bar{e} = \sqrt{TKE} = \sqrt{0.5(\sigma_u^2 + \sigma_v^2 + \sigma_w^2)}$, where σ_u^2 , σ_v^2 , and σ_w^2 are the variances of the three wind velocity components). Note that w_* and u_* have been used in previous studies to characterize the flux imbalance magnitude (e.g. their ratio was used by Huang et al., 2008).

In addition to k_{ec} , we also need an estimate of k_p , namely, the peak wavenumber. The peak wavenumber k_p can be related to the inverse of the integral length scale or $1/l$ (Kaimal and

Finnigan, 1994), which is an estimate of the size of organized turbulent structures in the turbulent boundary layer. It is defined based on the autocorrelation function R as follows:

$$l = \int_0^{\infty} R(r) dr, \quad (12)$$

where r is the displacement in space. In this study, l is calculated using the autocorrelation function of vertical velocity (l_w) or potential temperature (l_θ) with an integration until the first zero of $R(r)$ (Lenschow and Stankov, 1986). Note that because the average integral lengths are used in this study, the effects of oscillations of autocorrelation functions are small.

In a neutrally stratified atmospheric surface layer over homogenous surfaces, the integrate length scale is on the order of z (Kaimal et al., 1976), yielding that $[I]$ increases with $z/(uT)$. This result is in agreement with previous studies showing that the flux imbalance magnitude increases with increasing height in the surface layer, decreasing mean horizontal speed (when u is represented by the mean wind speed U), and shorter averaging period over homogeneous surfaces (Kanda et al., 2004; Steinfeld et al., 2007; Schalkwijk et al., 2016; Zhou et al., 2018). This agreement shows that the result from the conceptual model is reasonable (at least over homogeneous surfaces).

It is pointed out again that the relation between f_2 and k_{ec}/k_p is strongly dependent on the assumed cospectral shape (see Appendix B). That is, f_2 is not only a function of k_{ec}/k_p as Eq. (10) alludes to. While $l/(uT)$ might provide a good approximation to k_{ec}/k_p , other factors that can affect the cospectral shape (but not explicitly considered by the Massman and Clement (2005) model) need to be further considered. These factors include surface heterogeneity and atmospheric stability, the latter of which can be indicated by $-z_i/L$ where L is the Obukhov length. We choose $-z_i/L$ because previous studies (Lee et al, 2005; Moeng and Sullivan, 1994; Khanna and Brasseur, 1998; Schalkwijk et al., 2016) have found that $-z_i/L$ strongly affects large-scale turbulent coherent structures and thus the low wavenumber regime of the cospetra (Kaimal and Finnigan, 1994). For example, when $-z_i/L$ is larger than about 25, cell structures form with polygonal patterns and no noticeable alignment. When $-z_i/L$ is larger than 5 and smaller than 25, roll structures formed aligned with the wind (Lee et al, 2005). Moreover, previous studies have also found a correlation between the flux imbalance and $-z_i/L$ (Schalkwijk et al., 2016; Huang et al., 2008). Therefore, in this study, we use $-z_i/L$ to represent the effects of atmospheric stability on turbulent coherent structures and hence on the flux imbalance.

3 Experimental designs

3.1 Model description and configuration

We used the Weather Research and Forecasting (WRF) model version 3.9, which has the LES capability and has been widely used to investigate convective boundary layers over homogeneous and heterogeneous surfaces (Moeng et al., 2007; Talbot et al., 2012; Zhu et al., 2016). Following Zhu et al., (2016), the original WRF-LES model was modified so that the surface temperature, instead of the surface heat flux, can be prescribed as the surface boundary condition. We choose to do this because some recent studies (Basu et al., 2008; Holtslag et al., 2007) suggest that prescribing surface temperature is a better option than prescribing sensible heat flux under stable conditions. This is because the relation between surface heat flux and the temperature difference between the surface and the atmosphere is not monotonic under stable

conditions. As a result, prescribing surface heat flux could result in two physically sensible values for the friction velocity (and thus two different temperature gradients) and it is hard to determine which of these two values is more appropriate (Gibbs et al., 2014). While we do not study stable conditions in this paper, we aim to do so in the future. Hence, we decide to modify the WRF-LES model so that the surface temperature is prescribed from which the sensible heat flux is calculated.

Except for the surface layer scheme, other physical schemes in the WRF-LES model such as microphysics and radiation are all turned off. In the surface layer scheme, Monin-Obukhov similarity theory is used to calculate momentum flux and sensible heat flux from the prescribed surface temperature, with a parameterization for thermal roughness length (Chen and Dudhia, 2001) and the simulated air temperature assuming local homogeneity. Periodic boundary conditions are used in our simulations. In addition, we use the default WRF numerical discretization options (i.e., a fifth-order scheme for advection in the horizontal direction, a third-order scheme for advection in the vertical direction and a third-order Runge-Kutta scheme for the time integration). For the subgrid-scale turbulence parameterization, the 1.5-order turbulent kinetic energy-based closure scheme is used. The subgrid-scale flux is added to the turbulent flux. This is because the horizontal resolution used in our study (50 m) roughly corresponds to a sampling rate of 0.1 Hz, assuming a mean wind speed of 5 m/s. Hence the high-frequency temporal turbulent flux is only captured by the modelled spatial subgrid-scale flux.

The simulation domain is $5 \text{ km} \times 5 \text{ km} \times 2 \text{ km}$ in the x , y and z directions, respectively, and the number of grid points is $100 \times 100 \times 100$. Hence, the resolution in x - and y - directions is 50 m and ranges from 6 m - 20 m in the z -direction (i.e., using a vertically stretched grid, see Talbot et al., 2012). Note that due to the higher vertical resolution than the horizontal resolution especially near the surface, the anisotropic mixing option, where the length scales in horizontal and vertical directions are calculated separately in the subgrid-scale turbulence parameterization (i.e., the 1.5-order turbulent kinetic energy-based closure scheme), is selected to reduce the effects of large grid aspect ratio (see more details in Skamarock et al., 2008). The time step is 0.25 s. The model is initialized with an idealized neutral boundary-layer profile, in which the potential temperature is 298 K below 850 m, with a strong inversion layer of a potential temperature surge of 60 K km^{-1} from 850 to 1050 m. The potential temperature gradient is 3 K km^{-1} above 1050 m. All cases had the same initial atmospheric conditions. The geostrophic wind is set to be zero in all cases.

3.2 Numerical Experiments

In this study, we simulate a dry atmosphere over a heterogeneous surface composed of random configurations of patches with different surface temperatures and momentum roughness lengths. That is, we only consider the surface variations of surface temperature and momentum roughness length. We design two cases to analyze the effects of different heterogeneity scales on the flux imbalance. The key information is summarized in Table 2.

Similar to B07, a baseline surface configuration is created manually with relatively large patches (Fig. 2a). Subsequently, the baseline configuration is changed to create surfaces with different heterogeneity length scales. With different methods, two types of simulations are designed. The cases denoted by ‘B’ used the method from B07 (e.g., Eq. 3) and cases denoted by ‘H’ used the method from HM09 (e.g., Eq. 4). Due to the use of the same baseline configuration, the probability density functions (pdfs) of surface properties are identical in the two types of

simulations. However, due to the different surface pattern generation methods, the B cases and H cases are quite different (Fig. 2). For each type, four simulations are performed with different heterogeneity length scales (e.g., 2000 m, 1200 m, 550 m and 240 m). These scales are chosen to give a broad range of surface heterogeneity scales: one simulation with a heterogeneity scale larger than the boundary-layer height (2000 m), one simulation with a heterogeneity scale on the order of boundary-layer height (1200 m), and two simulations with heterogeneity scales smaller than the boundary-layer height (550 m and 240 m). The spatial patterns of surface temperature in the above mentioned simulations are shown in Fig. 2. The spatial patterns of momentum roughness lengths are shown in Appendix C (Fig. C1) because these spatial patterns are similar to the patterns of surface temperature. Note that the statistical properties (i.e., the pdfs) of surface temperatures and momentum roughness lengths in all cases are the same.

For all simulations, the temporal statistics (e.g., $\overline{w'\theta'}$) are calculated during a 1-hour integration period after a 2-hour spin-up (Patton et al., 2005) for all grid points, i.e., all the grids in the domain are virtual towers. Hence, the statistics are calculated over about 8 to 10 turnover times with the turnover time T_* is defined as z_i/w_* (Table 2). We then use Eq. (2) to compute the mean flux imbalance magnitude. Although the model time step is 0.25 s in our simulations, the output frequency is 1s. Due to the limitation of grid spacing, a higher sampling frequency does not resolve the turbulence better. For all simulations, the surface temperature is constant during the 3-hour integration time.

4 Results

4.1 The effects of surface heterogeneity scale on flux imbalance magnitude

4.1.1 The simulated ABL structures

As shown in Fig. 2, the patterns of surface temperature are significantly different between B cases and H cases. As a result, the sizes and spatial distributions of large eddies are different as shown in Fig. 3 and Fig. 4. In addition, the spatial patterns of large eddies clearly reflect the surface pattern, with updrafts concentrated above the hotter patches and downdrafts above the lower patches, especially when the surface heterogeneity scale is large (Fig. 3d and Fig. 3h), which is consistent with the results in De Roo and Mauder (2018). As the heterogeneity scale increases, larger organized structures are formed as shown in Fig. 3, which is similar to the results of HM09. Note that due to the larger organized structures with a 2000 m heterogeneity length in our domain (5 km \times 5 km), some parts of the domain start to behave locally homogeneous in B2000 and H2000 (Fig. 3 and Fig. 4).

Figure 5 shows the vertical profiles of mean potential temperature (θ), σ_u^2 , σ_w^2 , and TKE. The σ_u^2 and σ_w^2 are normalized by w_*^2 . Clearly, the cases with the smallest heterogeneity scales (B240 and H240) show structures of a well-mixed CBL. When the heterogeneity scale becomes larger, θ increases with height in the CBL, especially in cases B2000 and H2000. Similar results also occur in a larger domain (i.e., 10 km \times 10 km in Appendix D). This is in agreement with the results in Raasch and Harbusch (2001) and Avissar and Schmidt (1998), where the simulation domain ranges from 6 km to 40 km. One possible reason is that the asymmetry of circulation within the CBL, i.e., locally restricted updrafts and more extended weaker downdrafts (Deardorff et al., 1969), leads to an increase in θ with z within the CBL. Another possible reason is that when the surface heterogeneity scale is larger, the organized structures generated by the

surface heterogeneity have a larger probability to penetrate deeper into the inversion layer than the smaller eddies and hence warmer air is brought downward in the CBL by entrainment, which leads to the larger θ with higher height, especially when the surface heterogeneity scale is larger than z_i (Fig. 5a). Interestingly, different from the increase of potential temperature at the top of the boundary layer with increasing surface heterogeneity scales, the potential temperature near the surface decreases with the increasing surface heterogeneity scales. Hence, the potential temperature near the surface is the lowest in B2000 and H2000 simulations. The main reason is that near the ground surface, heat is mainly transferred into the atmosphere by relatively small eddies and hence the larger eddies caused by the entrainment due to the larger surface heterogeneity scales is somewhat detrimental to the mixing process, which leads to lower potential temperature near the surface (Avisar and Schmidt, 1998).

The vertical profiles of σ_u^2 and σ_w^2 indicate characteristics similar to many previous studies (Avisar and Schmidt, 1998; Patton et al., 2005; HM09). Namely, σ_u^2 increases near the surface and the entrainment zone; whereas, σ_w^2 reaches its maximum value in the middle of the mixed layer. As the heterogeneity scale becomes larger, σ_w^2 in $0 - 0.5 z_i$ becomes smaller, which is consistent with the results in HM09 and Patton et al. (2005). The explanation is that the larger surface heterogeneity scale, the more aggregated areas with stronger/weaker heat flux and hence more clearly separated regions with upward and downward eddies (Patton et al., 2005), which reduces the σ_w^2 with large surface heterogeneity scale. Similarly, in $0 - 0.5 z_i$ σ_u^2 generally decreases with increasing heterogeneity scale, which is different from the results in HM09 and Patton et al. (2005), where σ_u^2 increases with increasing surface heterogeneity scale. The free convective atmosphere instead of the shear convective atmosphere in HM09 may be responsible for this difference.

In addition, near the entrainment zone, σ_u^2 increases with increasing surface heterogeneity scale and reaches its maximum value at the heterogeneity scale of 2000 m, which is different from the trend near the surface. This discrepancy could be related to the observed correlation that the larger the surface heterogeneity scale, the larger perturbation induced by entrainment and hence the larger σ_u^2 (Fig. 5b). When the surface heterogeneity scale is larger than z_i , the effects of entrainment on σ_u^2 are maximum and can reach the surface, which leads to a larger σ_u^2 at the heterogeneity scale of 2000 m than that of 1200 m near the surface (Fig. 5b).

Due to the effects of entrainment, the height at which the largest σ_w^2 occurs also increases with increasing heterogeneity scale (Fig. 5c). For example, when the surface heterogeneity scales are smaller than z_i , the heights at which the largest σ_w^2 occur range from $0.3 - 0.4 z/z_i$, which is similar to previous studies (HM09; Patton et al., 2005). However, when the surface heterogeneity scales are larger than z_i , the heights at which the largest σ_w^2 occur can reach $0.6 - 0.7 z/z_i$, which is much larger than previous results (HM09; Patton et al., 2005). This large deviation is mainly caused by the fact that the larger surface heterogeneity scales, the more warm air is brought downward in the CBL by entrainment. Hence, the strong inversion layer in our LESs setup (see Sect. 3.1) acts as a source of heat at the top of the boundary layer, which behaves as an upside-down version of surface-driven turbulence (Hogan et al., 2009). That is why the heights at which the largest σ_w^2 occur can reach $0.6 - 0.7 z/z_i$ when the surface heterogeneity scales are larger than z_i . Meanwhile, due to the larger difference of entrainment rates among different simulations in case B than those in case H (Table 2), there are larger variations of σ_w^2 among different simulations in case B than those in case H (Fig. 5c).

The profile of TKE is affected by both σ_u^2 and σ_w^2 . In general, its value decreases with increasing heterogeneity scale (Fig. 5d). However, it should be noted that near the surface ($< 0.1 z_i$), the TKE is smallest in cases with heterogeneity scale of 1200 m instead of 2000 m due to the behavior of σ_u^2 .

Compared with H cases, θ is smaller in B cases, which is caused by the smaller surface heat fluxes in B cases (Table 2). Similar results can be also found in Avissar and Schmidt (1998).

4.1.2 The flux imbalance

Figure 6(a) shows the vertical profiles of flux imbalance magnitude calculated using Eq. (2) in different cases. Clearly, the flux imbalance magnitude increases with increasing height in both cases, which is consistent with previous studies (Kanda et al., 2004; Steinfeld et al., 2007; Huang et al., 2008; Zhou et al., 2018). It is also evident that the curves tend to cluster together at lower heights ($z/z_i < 0.02$). This is due to the fact that the parameterized subgrid-scale turbulence becomes important and the subgrid-scale flux dominates.

To examine the relation between the flux imbalance and the heterogeneity scale, the results at 112 m ($z/z_i \approx 0.08$) are shown as an example where the difference between the flux imbalance including the subgrid-scale heat flux and the flux imbalance excluding the subgrid-scale heat flux is less than 2% (Fig. 7). We choose to analyze the flux imbalance at a fixed z instead of a fixed z/z_i here because in practice all EC measurements have a fixed z . Overall the flux imbalance magnitude increases with increasing heterogeneity scales, as shown in Fig. 6b. This is consistent with field observations. For example, Stoy et al. (2013) and Xu et al. (2017) found that the flux imbalance magnitude increases with increasing landscape-level and footprint variability, respectively. This can be understood because the larger the heterogeneity scale is, the larger the circulations induced by surface heterogeneity become. These large-scale motions are less likely to be adequately sampled in a finite average period and hence a larger flux imbalance occurs.

Interestingly, when the heterogeneity scale becomes larger than z_i , the flux imbalance magnitude seems to decrease, especially in case B2000 (Fig. 6b). Close inspection of Fig. 6a reveals that this is the case nearly everywhere as long as $z/z_i > 0.02$. Such trends are even clearer with a larger domain (i.e., 10 km \times 10 km in Appendix D) and concomitantly larger patches. The further reduction of flux imbalance magnitude with increasing heterogeneity scale may be because the surface with a larger heterogeneity length starts to behave locally homogeneous.

In comparison, the flux imbalance magnitudes in B cases are generally larger than those in H cases. As discussed in Sect. 4.1.1, the smaller TKE and vertical turbulent heat flux induced by the more extended weaker downdraughts in B cases are responsible for this difference.

4.2 Interpretation of flux imbalance using the cospectral model

The cospectral model described in Sect. 2.3 connects the flux imbalance with f_1 and f_2 , where f_1 represents the ratio of “flux at height z ” to the surface flux and f_2 represents the role of large eddies in inducing flux imbalance. Specifically, the flux imbalance magnitude is expected to increase with decreasing f_1 and f_2 . In the following, we investigate the relations between flux

imbalance magnitude and f_1 and f_2 , as well as their controlling factors. It should be noted that here we do not assume any specific cospectral shapes but rather explore the relations between the computed f_1 and f_2 and flow variables.

4.2.1 f_1

As stated in Sect. 2.3, f_1 is calculated as $[\overline{w''\theta''}]/[\overline{HFX}]$ assuming that $\int_0^\infty F_{w\theta}(k, z) dk = [\overline{w''\theta''}]$ in Eq. (7). Figure 7(a) shows the calculated f_1 at different heights when the subgrid-scale heat flux is included. As can be seen, f_1 decreases with increasing heights in all cases when the subgrid-scale heat flux is included (Fig. 7a). Based on Eq. (10), the decrease of f_1 with increasing heights leads to the increase of flux imbalance magnitude, which is consistent with Fig. 6(a). However, there is virtually no difference between the two cases and also between simulations with different heterogeneity scales. As a result, Fig. 7(a) cannot explain the variations of flux imbalance with respect to heterogeneity scales (Fig. 6b).

Note again that f_1 has large uncertainty at lower heights due to the role of subgrid turbulence parameterization (c.f. Fig. 7a where the subgrid-scale heat flux is included and Fig. 7b where the subgrid-scale heat flux is excluded). For example, near the surface the f_1 values become even larger than 100% when the subgrid-scale flux is included (Fig. 7a), suggesting that the f_1 values at lower heights are less trustable. To avoid the effects of subgrid turbulence parameterization and large grid aspect ratios, we will focus on the results starting from a few grid levels above the surface, i.e., $0.03 z/z_i$ in our study, which is 50 m (equal to the horizontal resolution) above the surface corresponding the 9th grid level and where the percentage of the subgrid-scale flux is 6%. Therefore, in the following we will focus on the results in the range of $0.03 < z/z_i < 0.1$.

4.2.2 f_2

In this section, we examine the relation between f_2 and different turbulent length scales that might characterize k_{ec}/k_p . f_2 is inferred from $(1-[I])/f_1$ (Eq. 8), where $[I]$ and f_1 are calculated using Eq. (2) and $[\overline{w''\theta''}]/[\overline{HFX}]$ respectively. Note again that k_{ec} is the critical wavenumber of the EC method and we estimate k_{ec} as $1/(uT)$, where u is a velocity scale that can be represented U , w_* , u_* and \bar{e} , and T is the averaging period. Note that all velocity scales are first calculated locally and then averaged over the horizontal plane. The k_p is the peak wavenumber that might be estimated from the integral length scale of vertical velocity (l_w) or the integral length scale of potential temperature (l_θ). In the following we compare all these velocity and length scales.

Figure 8 shows the results in the range of $0.03 < z/z_i < 0.1$ when k_{ec}/k_p is represented by $l_w/(uT)$ with different velocity scales. One can see that f_2 generally decreases with increasing $l_w/(uT)$, consistent with Eq. (10), but with large scatter. Similar results are also found using $l_\theta/(uT)$ and hence those results are not shown. The large scatter suggests that additional variables (e.g., $-z_i/L$) should be considered to include the effects of atmospheric stability on turbulent coherent structures, which are not accounted for by Eq. (10). Similar to previous studies over homogeneous surfaces (Schalkwijk et al., 2016; Huang et al., 2008), we also found a reasonably strong correlation between the flux imbalance magnitude and $-z_i/L$ but over heterogeneous surfaces: the larger the $-z_i/L$, the smaller f_2 and thus the larger the flux imbalance magnitude (Fig. 9).

Therefore, we further examine the correlations between the f_2 and $-z_i/L \times l_w/(uT)$ (Fig. 10). The choice of $-z_i/L \times l_w/(uT)$ is motivated by the fact that the atmospheric stability is likely to influence the largest eddies and may be treated as an adjustable factor to k_p . Compared to Fig. 8, the negative correlations are much higher in Fig. 10 than those in Fig. 8 (see the R^2 values in Table 3). The better correlations confirm that $-z_i/L$ plays an important role in modulating the flux imbalance over heterogeneous surfaces.

Among all the velocity scales, using $-z_i/L \times l_w/(UT)$ yields the highest R^2 value (Table 3), indicating that the mean horizontal speed U better characterizes k_{ec} . On the other hand, using l_θ leads to quite peculiar relations and very larger scatter (and thus much smaller R^2 values, not shown here) compared to using l_w (Fig. 11), implying that l_w is a better choice to represent k_p at least in our cases.

4.2.3 A diagnostic equation for $[I]$

Given that the behavior of f_1 with z is quite predictable from Fig. 7, f_1 may be parameterized as follows:

$$f_1 = a \frac{z}{z_i} + b, \quad (13)$$

where $a = -1.46$ and $b = 1.0$ are fitted parameters (see the fitted line in Fig. 7). Again, to avoid the effect of subgrid turbulence parameterization, only data between in the range of $0.03 < z/z_i < 0.1$ are used to fit the parameters in Eq. (13). The linear decrease of turbulent heat flux in the CBL is a well-established result (Garratt, 1992), and our results confirm this. Note that we did not *a priori* specify the value of b . The fact that $b = 1.0$ is obtained from the fitting demonstrates that the linear decreasing trend in the range of $0.03 < z/z_i < 0.1$, when extrapolated to the surface, recovers the surface heat flux.

Similarly, given the nearly linear relationship between f_2 and $-z_i/L \times l_w/(UT)$ (here we use U due to the largest R^2 value it yields as shown in Table 3 and also the fact that its measurement is often available), we can parameterize f_2 as

$$f_2 = K \frac{z_i}{L} \frac{l_w}{UT} + C, \quad (14)$$

where $K = -0.05$ and $C = 0.95$ are fitted parameters (see the fitted line in Fig. 10a). Based on Eqs. (6), (13), (14), the flux imbalance magnitude can be parameterized as follows:

$$[I] = 1 - \left[a \frac{z}{z_i} + b \right] \left[K \frac{z_i}{L} \frac{l_w}{UT} + C \right]. \quad (15)$$

In practice, some of the inputs for Eq. (15) are not always available even if the coefficients a , b , K , and C are provided by fitting to LES results. For example, the calculation of z_i/L requires the boundary layer height and the surface heat flux. The former is rarely measured in the field while the latter is what the EC aims to measure and thus is unknown *a priori*. From this point view, Eq. (15) is a *diagnostic* equation and cannot be used as a *prognostic* equation to compute the flux imbalance. We note that this is also the case for other parameterizations in the literature (see e.g., Huang et al., 2008).

5 Discussions

5.1 The relation between the surface heterogeneity scale and flux imbalance

Our results demonstrate that the flux imbalance is primarily affected by the following variables: the integral length scale of vertical velocity l_w , the atmospheric stability parameter $-z_i/L$, the mean horizontal speed U , and the average period T , when the cospectral model is employed to interpret the flux imbalance. Among these four variables, l_w determines the maximum size of large-scale turbulent structures (i.e., the large eddies), $-z_i/L$ affects the shape of these turbulent structures and also the cospectrum form, i.e., the flux distribution among different eddy sizes, whereas U and T determine the number of large eddies that can be sampled by the EC sensors in a finite averaging period.

These characteristic variables are strongly affected by the surface heterogeneity. For example, one can infer from Fig. 9 that $-z_i/L$ is dependent on the surface heterogeneity scale. Figure 12a shows this more clearly. In addition, Fig. 12b shows the dependence of $l_w/(UT)$ on the surface heterogeneity scale. Due to the dependence of these characteristic variables on the surface heterogeneity scale, the flux imbalance is shown to be affected by surface heterogeneity in both our simulations (Fig. 6b) and previous observational studies (Stoy et al., 2013; Xu et al., 2017). Our results demonstrate that although the pdf of surface characteristics remains identical, landscapes with different characteristic length scales can have vastly different flux imbalance magnitude. This may explain why the relation between the surface heterogeneity and the flux imbalance observed in the field data shows large variability (Stoy et al., 2013; Xu et al., 2017).

5.2 The relations between the Eq. (15) and related factors

As stated in the introduction, previous studies have reported relations between flux imbalance and various factors (see Table 1). In this section, we use the conceptual model (i.e., Eq. 15) to explain these reported relations in the literature. Based on Eq. (15), it can be easily seen that the flux imbalance I increases with increasing z and $-z_i/L$, decreasing U (when u is represented by U) and TKE (when u is represented by TKE), and shorter T . Due to the increasing of I with z and $-z_i/L$, I also increases with the increasing of $-z/L$. In addition, as discussed in Sect. 5.1 and shown in Sect. 4.1.2 (Fig. 6b), overall the flux imbalance I increases with increasing surface heterogeneity scale. Because the $-z_i/L$ can be expressed as follows:

$$-\frac{z_i}{L} = k \left(\frac{w_*}{u_*} \right)^3, \quad (16)$$

where k is the von Kármán constant. Based on Eq. (16) and Eq. (15), we can also see that the flux imbalance I increases with decreasing u_*/w_* . These results inferred from our conceptual model are consistent with previous studies (see Table 1).

Furthermore, we can express Eq. (8) as follows:

$$f_2 = 1 - \frac{\int_0^{k_{ec}} F_{w\theta}(k, z) dk}{\int_0^\infty F_{w\theta}(k, z) dk} = 1 - \frac{1}{R_{w\theta}(z)\sigma(w)\sigma(\theta)} \int_0^{k_{ec}} F_{w\theta}(k, z) dk, \quad (17)$$

where $R_{w\theta}(z)$ is the correlation coefficient between w and θ at z ; $\sigma(w)$ and $\sigma(\theta)$ are standard deviations of w and θ , respectively. A larger phase difference between w and θ results in a

smaller $R_{w\theta}$ and thus a smaller f_2 (Eq. 17), which leads to a larger I based on Eq. (6). This conclusion is consistent with more recent results in McGloin et al. (2018) and Gao et al. (2017).

In summary, with the proposed diagnostic equation for I (i.e., Eq. 15), the relations between the flux imbalance and various factors reported in the literature (see Table 1) can be explained.

5.3 A comparison of different parameterizations for flux imbalance

Several energy balance closure parametrization schemes have been proposed (Panin et al., 1998; Huang et al., 2008; Panin and Bernhofer, 2008). An earlier comparison was made by Eder et al. (2014). In this paper, we also propose a conceptual model to explain the flux imbalance. Here, we compare these models and explain their advantages and limitations.

Based on LES runs over homogeneous surfaces, Huang et al. (2008) parametrized the flux imbalance as a function of non-dimensionalized turbulent velocity scales as

$$[I] = \left[\exp^{(a+b\frac{u_*}{w_*})} + c \right] \left[1.1 + d \left(\frac{z}{z_i} + f \right)^2 \right]^{0.5}, \quad (18)$$

where $a = 4.2$, $b = -16$, $c = 2.1$, $d = -8.0$ and $f = -0.38$ are fitted parameters. Zhou et al (2018) found the biggest shortcoming of this empirical parametrization scheme is that it cannot be applied directly to heterogeneous surfaces. Considering that surface heterogeneity is one of the main contributors to flux imbalance, the applicability of this parametrization scheme is greatly limited. In addition, this parameterization is developed based on LES data above the surface layer ($0.3 < z/z_i < 0.5$) and hence its applicability for analyzing real observations, which are mostly collected in the surface layer, is questionable, especially because the fitting function breaks down near the surface. This may be why field observations have reported failure of using this relation to capture flux imbalance (Eder et al., 2014). Lastly, as alluded to earlier, this parameterization cannot be used as a prognostic equation since one of the required inputs is the surface heat flux for computing w_* .

To consider the effect of surface heterogeneity on the flux imbalance, Panin and Bernhofer (2008) directly related the effective surface roughness length (z_0^{eff}) and surface heterogeneity scale (i.e., L^{eff}) to the flux imbalance and proposed the following parameterization

$$EBR = 1 - [I] = K \frac{z_0^{eff}}{L^{eff}} + C, \quad (19)$$

where EBR is the energy-balance closure ratio (the ratio of the sum of turbulent heat fluxes to the available energy), and K and C are empirical constants. Compared to the parameterization by Huang et al. (2008), the biggest advantage of this empirical parametrization scheme is that it explicitly considers the effects of surface heterogeneity and hence it can be used over heterogeneous surfaces. However, there are also some limitations associated with this parameterization. First, only the effect of momentum roughness length is included. Second, as shown in Fig. 6, even the same surface heterogeneity scale can yield very different flux imbalance magnitude. The large variation of flux imbalance magnitude suggests that the empirical constants (i.e., K and C) may be varying across sites and hence it is not surprising that the performance of this model also varies across sites (Eder et al., 2014). Last, the atmospheric stability and its interaction with surface heterogeneity can strongly affect turbulent organized

structures, which further alters the flux imbalance. Hence, only considering the surface heterogeneity scale solely based on the roughness length cannot correctly capture the flux imbalance under a variety of atmospheric stability conditions.

Compared to the previous two models, our model is derived from the cospectrum and hence is more physically based. It should be pointed out that the surface heterogeneity scale is not explicit in our model. This is because the model is constructed based on the assumption that large-scale organized turbulent structures lead to the flux imbalance. The effect of surface heterogeneity on flux imbalance is implicitly included in our model by considering the impact of surface heterogeneity on characteristic variables of turbulent flows, especially those related to large eddies.

There are also some limitations of our model. Most importantly, our model is based on the assumption that the flux imbalance is only caused by the large eddies. Therefore, the flux imbalance caused by other factors cannot be explained by our model. In addition, our model is also a diagnostic model and cannot be directly applied in practice to calculate the flux imbalance. Lastly, our model is constructed with data in the range $0.03 < z/z_i < 0.1$. While this range is much lower than that in Huang et al. (2008), the lowest limit ($z/z_i = 0.03$) is still higher than the typical measurement height in the field. Whether our model can capture the behavior of flux imbalance near the surface ($z/z_i < 0.03$) needs to be investigated using higher-resolution LESs in the future.

5.4 A comparison between our model and the existing cospectral corrections in EC

The proposed conceptual model is similar to the cospectral corrections already applied in the EC post-processing (Massman and Clement, 2005). However, there are key differences between our model and the existing cospectral corrections. First of all, the proposed model is only used to better understand the flux imbalance and to explore the flow and surface variables that affect the flux imbalance. We do not intend to use it for calculations or corrections of the flux imbalance for two reasons: First, the low wavenumber range of the cospectrum is strongly affected by boundary conditions (Fig. 1; Kaimal and Finnigan, 1994). Most cospectral models (see Appendix B) are derived from data collected over homogeneous surfaces. Hence, their shapes, especially in the low wavenumber range, are likely to be different over heterogeneous surfaces. It is also noted that these cospectral models are mostly for the one-dimensional cospectrum, i.e., they only have a radial dependence, which excludes the effects of azimuthal variability of the surface on the cospectrum. Second, it remains unclear which factors best capture the k_{ec} and k_p , although we parameterize the k_{ec} and k_p using $1/(uT)$ and $1/l$, respectively in our study. Therefore, it remains to be investigated whether and how our results can be applied to correct the missing low-frequency flux in the EC observation.

Moreover, our proposed model only considers the flux imbalance due to the large eddies while the cospectral corrections of the post-processing of EC data consider the flux imbalance due to not only the low-frequency loss but more importantly the high-frequency loss. In addition, although our model and existing corrections consider the effects of low-frequency eddies or large eddies, the transfer functions are different. Our model is based on the spatial cospectrum and hence a sharp or step transfer function, which is equal to 0 below k_{ec} and is equal to 1 above k_{ec} , can be directly applied. However, the cospectral corrections already applied in the EC post-processing are based on the temporal cospectrum. Although simple time windows or sharp cut-offs can be applied in time domain, their Fourier transforms rarely have transfer functions that provide sharp cut-offs in the frequency domain (see Fig. 2.2 in Moncrieff et al., 2005).

Lastly, the “true flux” (or “reference flux”) is different between our proposed model and the cospectral corrections already applied in the EC post-processing. For example, in our proposed model the “true flux” is the surface heat flux while in the spectral corrections the “true cospectrum” is the flux obtained from the standard cospectrum (e.g., the Kansas cospectrum, Haugen et al., 1971). Since the low wavenumber range of cospectrum is strongly affected by boundary conditions, the cospectrum obtained from the Kansas experiment may not be applicable elsewhere, which may be why flux imbalance still occurs after the spectral corrections are applied in the post-processing of EC data.

6 Conclusions

This study analyzes the relationship between the surface heterogeneity scale and the flux imbalance over heterogeneous landscapes under free convective conditions. The main conclusions are summarized as follows:

(1) The surface heterogeneity scale strongly affects the flux imbalance even when the pdfs of surface characteristics are the same. The flux imbalance magnitude initially increases with increasing surface heterogeneity scale. When the surface heterogeneity scale becomes larger than the boundary-layer height, the surface starts to behave locally homogeneous, which leads to a lower flux imbalance.

(2) A conceptual model for the flux imbalance is proposed to better understand the flux imbalance induced by the large eddies. Based on this conceptual model, we find that the flux imbalance is controlled by $-z_i/L$, l_w , U , and T . Among these three variables, the l_w determines the maximum size of large eddies; the $-z_i/L$ represents the form of these large eddies or the cospectrum form, i.e., the flux distribution among different eddy sizes; the U and T determine how many these large eddies can be sampled by the EC in a finite averaging period.

(3) Assuming that the flux imbalance is mainly caused by the inadequate sampling of large eddies, a diagnostic equation for the average flux imbalance magnitude is proposed as $[I] = 1 - [az/z_i + b][-K \times z_i/L \times l_w/UT + C]$, where a , b , K , and C are empirical constants and b should in theory equal to unity. Compared to the other empirical and semi-empirical models, our model is derived from the cospectrum and hence is more physically based. Moreover, the qualitative relations between the flux imbalance and various factors reported in the literature can be explained by our model. Note that our model is diagnostic because it requires *a priori* knowledge of the surface heat flux. In addition, it also requires boundary-layer height as an input, which is not always available. It is also pointed out that this model is constructed with data in the range $0.03 < z/z_i < 0.1$.

Our study has a few limitations. First, it is important to point out that our study does not consider latent heat flux, whose behavior might be different from that of sensible heat flux, especially in the low frequency (Cava et al., 2008; Detto et al., 2008; Huang et al., 2009; Li and Bou-Zeid, 2011; Li et al., 2012; Cancelli et al., 2014; Charuchittipan et al., 2014; Gao et al., 2017). Second, we only examine the flux imbalance under free convective conditions. As found by previous studies (e.g., Steinfeld et al., 2007; Huang et al., 2008; Schalkwijk et al., 2016; Zhou et al., 2018), the geostrophic winds have important effects on the flux imbalance. However, it remains a challenge to conduct LESs with geostrophic winds over heterogeneous surfaces. That is, it is problematic to use a periodical boundary condition over two-dimensional heterogeneous surfaces when the geostrophic wind exists. To avoid or reduce the effects of periodical boundary

conditions on the results, buffer zones around the study area are needed (e.g., Maronga and Raasch, 2013; Liu et al., 2018). The sizes of buffer zones increase with increasing geostrophic winds and hence the buffer zones may be much larger than the study area with a large geostrophic wind, which will lead to a heavy computational burden. Moreover, the buffer zones could also induce additional large eddies, which further contributes to the flux imbalance. Therefore, how to set up the surface values over these buffer zones is also important. In summary, not only the sizes of buffer zones but also the surface values over these buffer zones have effects on the flux imbalance, which needs to be explored in the future. Last, only the domain averaged flux imbalance instead of the flux imbalance at one point is explored due to the use of coarse resolution LESs in this study. Hence, how our results are applied to correcting the EC non-closure at one point in the field needs to be investigated in the future.

Appendix A: The derivation of Eq. (10)

In this appendix, the flux imbalance is deduced by using the cospectral model of Massman and Clement (2005), which can be expressed as follows:

$$F_{w\theta}(k) = \frac{A_{w\theta}}{k_p \left[1 + m_{w\theta} \left(\frac{k}{k_p} \right)^{2\mu} \right]^{\frac{1}{2\mu} \times \frac{m_{w\theta}+1}{m_{w\theta}}}}, \quad (20)$$

where $A_{w\theta}$ is a normalization parameter, k_p is the peak wavenumber, and $m_{w\theta}$ and μ are the (inertial subrange) slope parameter and broadness parameter, respectively. Substituting Eq. 20 into the Eq. (8), the flux imbalance can be expressed as:

$$f_2 = 1 - \frac{\frac{D\Gamma\left(\frac{1}{2\mu}, 0\right) - D\Gamma\left(\frac{1}{2\mu}, \frac{m+1}{2\mu} \left(\frac{k_{ec}}{k_p}\right)^{2\mu}\right)}{(1+m)^{\frac{1}{2\mu}}}}{\frac{D\Gamma\left(\frac{1}{2\mu}, 0\right)}{(1+m)^{\frac{1}{2\mu}}}} = \frac{\Gamma\left(\frac{1}{2\mu}, \frac{m+1}{2\mu} \left(\frac{k_{ec}}{k_p}\right)^{2\mu}\right)}{\Gamma\left(\frac{1}{2\mu}, 0\right)}, \quad (21)$$

where

$$D = 2^{\frac{1}{2\mu}-1} a \mu^{\frac{1}{2\mu}-1}, \quad (22)$$

$$\Gamma(s, x) = \int_x^\infty t^{s-1} e^{-t} dt. \quad (23)$$

Eq. (21) is identical to the Eq. (10) in the main text. Due to the decrease of $\Gamma(s, x)$ with increasing x , f_2 is expected to decrease as k_{ec}/k_p increases.

Appendix B: Different cospectral models and the derived f_2

In this appendix, different cospectral models are used to derive the flux imbalance.

1. The cospectral model of Katul et al. (2013)

Katul et al. (2013) provided a simple cospectral model, which can be expressed as follows:

$$F_{w\theta}(k) = \begin{cases} \frac{\varepsilon^{-\frac{1}{3}} k_p^{-\frac{7}{3}}}{C_1} \{dT C_{ww} + (1 - C_2) \beta C_{\theta\theta}\}, & k > k_p \\ \frac{\varepsilon^{-\frac{1}{3}} k^{-\frac{7}{3}}}{C_1} \{dT C_{ww} + (1 - C_2) \beta C_{\theta\theta}\}, & k \leq k_p \end{cases}, \quad (24)$$

where ε is the TKE dissipation rate; k_p is the peak wavenumber; dT and β are the air temperature gradient and buoyancy parameter, respectively; and C_2 , C_{ww} and $C_{\theta\theta}$ are constants. Substituting Eq. (24) into the Eq. (8), the flux imbalance leads to:

$$f_2 = 1 - \frac{\frac{k_{ec} \varepsilon^{-\frac{1}{3}} k_p^{-\frac{7}{3}}}{C_1} \{\Gamma C_{ww} + (1 - C_2) \beta C_{\theta\theta}\}}{\frac{7}{4} k_p^{-\frac{4}{3}} \frac{\varepsilon^{-\frac{1}{3}}}{C_1} \{\Gamma C_{ww} + (1 - C_2) \beta C_{\theta\theta}\}} = 1 - \frac{4}{7} \frac{k_{ec}}{k_p}. \quad (25)$$

Clearly, f_2 decreases with increasing k_{ec}/k_p .

2. The cospectral model of Massom and Lee (2002)

Massom and Lee (2002) gave another simple expression for cospectrum:

$$F_{w\theta}(k) = \frac{2}{\pi} \frac{1}{k_p [1 + (k/k_p)]^2}. \quad (26)$$

Substituting Eq. (26) into Eq. (8), f_2 can be expressed as follows:

$$f_2 = \frac{1}{\left(1 + \frac{k_{ec}}{k_p}\right)}. \quad (27)$$

It is clear that in this model f_2 also decreases with increasing k_{ec}/k_p .

Appendix C: The spatial patterns of momentum roughness lengths

Appendix D: The effect of domain size on the results

In order to examine the effect of domain size on our results, we add an additional case, i.e., case D where all parameters are identical to case B except with a larger domain (i.e., 10 km \times 10 km). The patches are also enlarged concomitantly so the heterogeneity scale is doubled. Clearly, we can see that in the large domain (Figs. D1 and D2), the results are similar to those in the main paper, suggesting that the main findings of our main paper are not sensitive to the domain size.

Acknowledgments

This work was jointly supported by the Strategic Priority Research Program of the Chinese Academy of Sciences (Grant No. XDA20100104), the National Natural Science Foundation of China (Grant No. 91425303 and 41630856), and the 13th Five-year Informatization Plan of Chinese Academy of Sciences (Grant No. XXH13505-06). The authors declare that they have no conflict of interest. All data used in this study can be obtained from the Environmental and Ecological Science Data Center for West China (<http://westdc.westgis.ac.cn>).

References

- Albertson, J. D., W. P. Kustas, and T. M. Scanlon (2001), Large-eddy simulation over heterogeneous terrain with remotely sensed land surface conditions, *Water Resources Research*, 37(7), 1939-1953, doi: 10.1029/2000wr900339.
- Aubinet, M., T. Vesala, and D. Papale (2012), Eddy Covariance, in *A Practical Guide to Measurement and Data Analysis*, edited by M. Aubinet, T. Vesala and D. Papale, p. 442, Springer, Dordrecht, Heidelberg, London, New York, doi:0.1007/978-94-007-2351-1.
- Avissar, R., and T. Schmidt (1998), An evaluation of the scale at which ground-surface heat flux patchiness affects the convective boundary layer using large-eddy simulations, *Journal of the Atmospheric Sciences*, 55(16), 2666-2689, doi:10.1175/1520-0469(1998)055<2666:aeotsa>2.0.co;2.
- Baldocchi, D., et al. (2001), FLUXNET: A new tool to study the temporal and spatial variability of ecosystem-scale carbon dioxide, water vapor, and energy flux densities, *Bulletin of the American Meteorological Society*, 82(11), 2415-2434, doi:10.1175/1520-0477(2001)082<2415:Fantts>2.3.Co;2.
- Basu, S., A. Holtslag, B. Wiel, A. Moene, and G.-J. Steeneveld (2008), An inconvenient “truth” about using sensible heat flux as a surface boundary condition in models under stably stratified regimes, *Acta Geophysica*, 56(1), 88–99, doi:10.2478/s11600-007-0038-y.
- Bertoldi, G., J. D. Albertson, W. P. Kustas, F. Li, and M. C. Anderson (2007), On the opposing roles of air temperature and wind speed variability in flux estimation from remotely sensed land surface states, *Water Resources Research*, 43(10), W10433, doi:10.1029/2007wr005911.
- Bou-Zeid, E., M. B. Parlange, and C. Meneveau (2007), On the parameterization of surface roughness at regional scales, *Journal of the Atmospheric Sciences*, 64(1), 216-227, doi:10.1175/Jas3826.1.
- Cancelli, D. M., M. Chamecki, and N. L. Dias (2014), A Large-Eddy Simulation Study of Scalar Dissimilarity in the Convective Atmospheric Boundary Layer, *Journal of the Atmospheric Sciences*, 71(1), 3-15, doi:10.1175/jas-d-13-0113.1.
- Charuchittipan, D., W. Babel, M. Mauder, J.-P. Leps, and T. Foken (2014), Extension of the averaging time in eddy-covariance measurements and its effect on the energy balance closure, *Boundary-Layer Meteorology*, 152(3), 303-327, doi:10.1007/s10546-014-9922-6.

- Chen, F., and R. Avissar (1994), The impact of land-surface wetness heterogeneity on mesoscale heat fluxes, *Journal of Applied Meteorology*, 33(11), 1323-1340, doi:10.1175/1520-0450(1994)033<1323:tiolsw>2.0.co;2.
- Chen, F., and J. Dudhia (2001), Coupling an Advanced Land Surface–Hydrology Model with the Penn State–NCAR MM5 Modeling System. Part I: Model Implementation and Sensitivity, *Monthly Weather Review*, 129(4), 569-585, doi:10.1175/1520-0493(2001)129<0569:CAALSH>2.0.CO;2.
- Chen, J., S. Fan, C. Zhao, X. Xiao, X. Cai, and H. Liu (2006), The underestimation of the turbulent fluxes in eddy correlation techniques, *Chinese Journal of Atmospheric Sciences*, 30(3), 423-432, doi:10.3878/j.issn.1006-9895.2006.03.06. (in Chinese)
- De Roo, F., and M. Mauder (2018), The influence of idealized surface heterogeneity on virtual turbulent flux measurements, *Atmospheric Chemistry and Physics*, 18(7), 5059-5074, doi:10.5194/acp-18-5059-2018.
- Deardorff, J. W., G. E. Willis, and D. K. Lilly (1969), Laboratory investigation of non-steady penetrative convection, *Journal of Fluid Mechanics*, 35, 7-31, doi:10.1017/S0022112069000942.
- Dennis, D. J. C., and T. B. Nickels (2008), On the limitations of Taylor's hypothesis in constructing long structures in a turbulent boundary layer, *Journal of Fluid Mechanics*, 614, 197-206, doi:10.1017/S0022112008003352.
- Detto, M., G. Katul, M. Mancini, N. Montaldo, and J. D. Albertson (2008), Surface heterogeneity and its signature in higher-order scalar similarity relationships, *Agricultural and Forest Meteorology*, 148(6-7), 902-916, doi:10.1016/j.agrformet.2007.12.008.
- Eder, F., F. De Roo, K. Kohnert, R. L. Desjardins, H. P. Schmid, and M. Mauder (2014), Evaluation of two energy balance closure parametrizations, *Boundary-Layer Meteorology*, 151(2), 195-219, doi:10.1007/s10546-013-9904-0.
- Eder, F., M. Schmidt, T. Damian, K. Trautner, and M. Mauder (2015a), Mesoscale eddies affect near-surface turbulent exchange: evidence from lidar and tower measurements, *Journal of Applied Meteorology and Climatology*, 54(1), 189-206, doi:10.1175/Jamc-D-14-0140.1.
- Eder, F., F. De Roo, E. Rotenberg, D. Yakir, H. P. Schmid, and M. Mauder (2015b), Secondary circulations at a solitary forest surrounded by semi-arid shrubland and their impact on eddy-covariance measurements, *Agricultural and Forest Meteorology*, 211, 115-127, doi:10.1016/j.agrformet.2015.06.001.
- Finnigan, J. J., R. Clement, Y. Malhi, R. Leuning, and H. A. Cleugh (2003), A re-evaluation of long-term flux measurement techniques - Part I: Averaging and coordinate rotation, *Boundary-Layer Meteorology*, 107(1), 1-48, doi:10.1023/A:1021554900225.
- Foken, T. (2008), The energy balance closure problem: An overview, *Ecological Applications*, 18(6), 1351-1367, doi:10.1890/06-0922.1.
- Foken, T., M. Aubinet, J. J. Finnigan, M. Y. Leclerc, M. Mauder, and K. T. P. U (2011), Results of a panel discussion about the energy balance closure correction for trace gases, *Bulletin of the American Meteorological Society*, 92(4), Es13-Es18, doi:10.1175/2011bams3130.1.

- Foken, T., F. Wimmer, M. Mauder, C. Thomas, and C. Liebethal (2006), Some aspects of the energy balance closure problem, *Atmospheric Chemistry and Physics*, 6, 4395-4402.
- Franssen, H. J. H., R. Stöckli, I. Lehner, E. Rotenberg, and S. I. Seneviratne (2010), Energy balance closure of eddy-covariance data: A multisite analysis for European FLUXNET stations, *Agricultural and Forest Meteorology*, 150(12), 1553-1567, doi:10.1016/j.agrformet.2010.08.005.
- Gao, Z. M., H. P. Liu, G. K. Katul, and T. Foken (2017), Non-closure of the surface energy balance explained by phase difference between vertical velocity and scalars of large atmospheric eddies, *Environmental Research Letters*, 12(3), 034025, doi:10.1088/1748-9326/aa625b.
- Gao, Z.Q., R. Horton, and H. P. Liu (2010), Impact of wave phase difference between soil surface heat flux and soil surface temperature on soil surface energy balance closure, *Journal of Geophysical Research-Atmospheres*, 115, D16112, doi:10.1029/2009jd013278.
- Garratt JR (1992) *The atmospheric boundary layer*. Cambridge University Press, UK 316 pp
- Gibbs, J. A., E. Fedorovich, and A. Shapiro (2014), Revisiting surface heat-flux and temperature boundary conditions in models of stably stratified boundary-layer flows, *Boundary-Layer Meteorology*, 154(2), 171–187, doi:10.1007/s10546-014-9970-y.
- Haugen, D. A., J. C. Kaimal, and E. F. Bradley (1971), An experimental study of Reynolds stress and heat flux in the atmospheric surface layer, *Quarterly Journal of the Royal Meteorological Society*, 97(412), 168-180, doi:10.1002/qj.49709741204.
- Hogan, R. J., A. L. M. Grant, A. J. Illingworth, G. N. Pearson, and E. J. O'Connor (2009), Vertical velocity variance and skewness in clear and cloud-topped boundary layers as revealed by Doppler lidar, *Quarterly Journal of the Royal Meteorological Society*, 135(640), 635-643, doi:10.1002/qj.413.
- Holtstlag, A.A.M., G.J. Steeneveld, and B.J.H. van de Wiel (2007), Role of land-surface temperature feedback on model performance for the stable boundary layer. *Boundary-Layer Meteorology*, 125, 361-376, doi:10.1007/s10546-007-9214-5.
- Huang, H.-Y., and S. A. Margulis (2009), On the impact of surface heterogeneity on a realistic convective boundary layer, *Water Resources Research*, 45(4), W04425, doi:10.1029/2008WR007175.
- Huang, J. P., X. H. Lee, and E. G. Patton (2008), A modelling study of flux imbalance and the influence of entrainment in the convective boundary layer, *Boundary-Layer Meteorology*, 127(2), 273-292, doi:10.1007/s10546-007-9254-x.
- Huang, J. P., X. H. Lee, and E. G. Patton (2009), Dissimilarity of scalar transport in the convective boundary layer in inhomogeneous landscapes, *Boundary-Layer Meteorology*, 130(3), 327-345, doi:10.1007/s10546-009-9356-8.
- Inagaki, A., M. O. Letzel, S. Raasch, and M. Kanda (2006), Impact of surface heterogeneity on energy imbalance: A study using LES, *Journal of the Meteorological Society of Japan*, 84(1), 187-198, doi:10.2151/jmsj.84.187.
- Jung, M., M. Reichstein, P. Ciais, S. I. Seneviratne, J. Sheffield, M. L. Goulden, G. Bonan, A. Cescatti, J. Chen, and R. De Jeu (2010), Recent decline in the global land

- evapotranspiration trend due to limited moisture supply, *Nature*, 467(7318), 951-954, doi:10.1038/nature09396.
- Kaimal, J. C., J. C. Wyngaard, D. A. Haugen, O. R. Coté, Y. Izumi, S. J. Caughey, and C. J. Readings (1976), Turbulence structure in the convective boundary layer, *Journal of the Atmospheric Sciences*, 33(11), 2152-2169, doi:10.1175/1520-0469(1976)033<2152:tsitcb>2.0.co;2.
- Kaimal J. C., and J. J. Finnigan (1994) *Atmospheric boundary layer flows: their structure and measurement*. Oxford University Press, New York, 289 pp
- Kanda, M., A. Inagaki, M. O. Letzel, S. Raasch, and T. Watanabe (2004), LES study of the energy imbalance problem with eddy covariance fluxes, *Boundary-Layer Meteorology*, 110(3), 381-404, doi:DOI 10.1023/B:BOUN.0000007225.45548.7a.
- Katul, G. G., A. Porporato, C. Manes, and C. Meneveau (2013), Co-spectrum and mean velocity in turbulent boundary layers, *Physics of Fluids*, 25(9), 091702, doi:10.1063/1.4821997.
- Khanna, S., and J. G. Brasseur (1998), Three-dimensional buoyancy- and shear-induced local structure of the atmospheric boundary layer, *Journal of the Atmospheric Sciences*, 55(5), 710-743, doi:10.1175/1520-0469(1998)055<0710:tdbasi>2.0.co;2.
- Kustas, W. P., and J. D. Albertson (2003), Effects of surface temperature contrast on land-atmosphere exchange: A case study from Monsoon 90, *Water Resources Research*, 39(6), 1159, doi:10.1029/2001wr001226.
- Lee, X. H. (1998), On micrometeorological observations of surface-air exchange over tall vegetation, *Agricultural and Forest Meteorology*, 91(1-2), 39-49, doi:10.1016/S0168-1923(98)00071-9.
- Lee, X. H., W. Massman, and B. Law (2005), *Handbook of micrometeorology-A guide for surface flux measurement and analysis*, 250 pp., Springer Netherlands, doi:10.1007/1-4020-2265-4.
- Lenschow, D. H., and B. B. Stankov (1986), Length scales in the convective boundary layer, *Journal of the Atmospheric Sciences*, 43(12), 1198-1209, doi:10.1175/1520-0469(1986)043<1198:Lsitcb>2.0.Co;2.
- Leuning, R., E. van Gorsel, W. J. Massman, and P. R. Isaac (2012), Reflections on the surface energy imbalance problem, *Agricultural and Forest Meteorology*, 156, 65-74, doi:10.1016/j.agrformet.2011.12.002.
- Li, D., and E. Bou-Zeid (2011), Coherent structures and the dissimilarity of turbulent transport of momentum and scalars in the unstable atmospheric surface layer, *Boundary-Layer Meteorology*, 140(2), 243-262, doi:10.1007/s10546-011-9613-5.
- Li, D., E. Bou-Zeid, and H. A. R. De Bruin (2012), Monin-Obukhov similarity functions for the structure parameters of temperature and humidity, *Boundary-Layer Meteorology*, 145(1), 45-67, doi:10.1007/s10546-011-9660-y.
- Li, D., and G. G. Katul (2017), On the linkage between the $k^{-5/3}$ spectral and $k^{-7/3}$ cospectral scaling in high-Reynolds number turbulent boundary layers, *Physics of Fluids*, 29(6), 065108, doi:10.1063/1.4986068.

- Li, X., et al. (2013), Heihe Watershed Allied Telemetry Experimental Research (HiWATER): Scientific Objectives and Experimental Design, *Bulletin of the American Meteorological Society*, 94(8), 1145-1160, doi:10.1175/Bams-D-12-00154.1.
- Li, X., K. Yang, and Y. Z. Zhou (2016), Progress in the study of oasis-desert interactions, *Agricultural and Forest Meteorology*, 230-231, 1-7, doi:10.1016/j.agrformet.2016.08.022.
- Li, X., et al. (2017), A multiscale dataset for understanding complex eco-hydrological processes in a heterogeneous oasis system, *Scientific Data*, 4, 1-11, doi:10.1038/sdata.2017.83.
- Li, Z. Q., G. R. Yu, X. F. Wen, L. M. Zhang, C. Y. Ren, and Y. L. Fu (2005), Energy balance closure at ChinaFLUX sites, *Science in China Series D-Earth Sciences*, 48, 51-62, doi:10.1360/05zd0005.
- Liu, S. F., Y. P. Shao, A. Kunoth, and C. Simmer (2017), Impact of surface-heterogeneity on atmosphere and land-surface interactions, *Environmental Modelling & Software*, 88, 35-47, doi:10.1016/j.envsoft.2016.11.006.
- Lumley, J. L. (1967), Similarity and the Turbulent Energy Spectrum, *Physics of Fluids*, 10(4), 855-858, doi:10.1063/1.1762200.
- Mahrt, L. (1998), Flux sampling errors for aircraft and towers, *Journal of Atmospheric and Oceanic Technology*, 15(2), 416-429, doi:10.1175/1520-0426(1998)015<0416:Fsefaa>2.0.Co;2.
- Massman, W. J., and X. Lee (2002), Eddy covariance flux corrections and uncertainties in long-term studies of carbon and energy exchanges, *Agricultural and Forest Meteorology*, 113(1-4), 121-144, doi:10.1016/S0168-1923(02)00105-3.
- Massman, W. J., and R. Clement (2005), Uncertainty in eddy covariance flux estimates resulting from spectral attenuation. In X Lee, W Massman, and B Law, editors, *Handbook of Micrometeorology*. Springer, Dordrecht.
- McGloin, R., L. Šigut, K. Havránková, J. Dušek, M. Pavelka, and P. Sedlák (2018), Energy balance closure at a variety of ecosystems in Central Europe with contrasting topographies, *Agricultural and Forest Meteorology*, 248, 418-431, doi:10.1016/j.agrformet.2017.10.003.
- Moeng, C. H., and P. P. Sullivan (1994), A comparison of shear-driven and buoyancy-driven planetary boundary-layer flows, *Journal of the Atmospheric Sciences*, 51(7), 999-1022, doi:10.1175/1520-0469(1994)051<0999:Acosab>2.0.Co;2.
- Moeng, C. H., J. Dudhia, J. Klemp, and P. Sullivan (2007), Examining two-way grid nesting for large eddy simulation of the PBL using the WRF model, *Monthly Weather Review*, 135(6), 2295-2311, doi:10.1175/Mwr3406.1.
- Moncrieff, J., R. Clement, J. J. Finnigan, and T. Meyers (2005), Averaging, detrending, and filtering of eddy covariance time series. In X Lee, W Massman, and B Law, editors, *Handbook of Micrometeorology*. Springer, Dordrecht.
- Moore, C. J. (1986), Frequency-response corrections for eddy-correlation systems, *Boundary-Layer Meteorology*, 37(1-2), 17-35, doi:10.1007/Bf00122754.

- 879 Oncley, S. P., et al. (2007), The Energy Balance Experiment EBEX-2000. Part I: Overview and
880 energy balance, *Boundary-Layer Meteorology*, 123(1), 1-28, doi:10.1007/s10546-007-
881 9161-1.
- 882 Panin, G. N., and C. Bernhofer (2008), Parametrization of turbulent fluxes over inhomogeneous
883 landscapes, *Izvestiya Atmospheric and Oceanic Physics*, 44(6), 701-716,
884 doi:10.1134/S0001433808060030.
- 885 Panin, G. N., G. Tetzlaff, and A. Raabe (1998), Inhomogeneity of the land surface and problems
886 in the parameterization of surface fluxes in natural conditions, *Theoretical and Applied*
887 *Climatology*, 60(1-4), 163-178, doi:10.1007/s007040050041.
- 888 Patton, E. G., P. P. Sullivan, and C.-H. Moeng (2005), The influence of idealized heterogeneity
889 on wet and dry planetary boundary layers coupled to the land surface, *Journal of the*
890 *Atmospheric Sciences*, 62(7), 2078-2097, doi:10.1175/jas3465.1.
- 891 Raasch, S., and G. Harbusch (2001), An analysis of secondary circulations and their effects
892 caused by small-scale surface inhomogeneities using large-eddy simulation, *Boundary-*
893 *Layer Meteorology*, 101(1), 31-59, doi:10.1023/A:1019297504109.
- 894 Schalkwijk, J., H. J. J. Jonker, and A. P. Siebesma (2016), An investigation of the eddy-
895 covariance flux imbalance in a year-long large-eddy simulation of the weather at Cabauw,
896 *Boundary-Layer Meteorology*, 160(1), 17-39, doi:10.1007/s10546-016-0138-9.
- 897 Skamarock, W. C., et al. (2008), A description of the advanced research WRF version 3. NCAR
898 Technical Note NCAR/TN-475+STR, doi:10.5065/D68S4MVH.
- 899 Steinfeld, G., M. O. Letzel, S. Raasch, M. Kanda, and A. Inagaki (2007), Spatial
900 representativeness of single tower measurements and the imbalance problem with eddy-
901 covariance fluxes: results of a large-eddy simulation study, *Boundary-Layer Meteorology*,
902 123(1), 77-98, doi:10.1007/s10546-006-9133-x.
- 903 Stoy, P. C., et al. (2013), A data-driven analysis of energy balance closure across FLUXNET
904 research sites: The role of landscape scale heterogeneity, *Agricultural and Forest*
905 *Meteorology*, 171, 137-152, doi:10.1016/j.agrformet.2012.11.004.
- 906 Stull, R. B. (1988), *An Introduction to Boundary Layer Meteorology*, Springer Science &
907 Business Media, Dordrecht, Netherlands. 670 pp.
- 908 Talbot, C., E. Bou-Zeid, and J. Smith (2012), Nested mesoscale large-eddy simulations with
909 WRF: performance in real test cases, *Journal of Hydrometeorology*, 13(5), 1421-1441,
910 doi:10.1175/jhm-D-11-048.1.
- 911 Twine, T. E., W. Kustas, J. Norman, D. Cook, P. Houser, T. Meyers, J. Prueger, P. Starks, and
912 M. Wesely (2000), Correcting eddy-covariance flux underestimates over a grassland,
913 *Agricultural and Forest Meteorology*, 103(3), 279-300, doi:10.1016/S0168-1923(00)00123-
914 4.
- 915 Wang, J. M., W. Z. Wang, S. M. Liu, M. G. Ma, and X. Li (2009), The Problems of Surface
916 Energy Balance Closure: An Overview and Case Study, *Advance in Earth Sciences*, 24(7),
917 705-713, doi:10.11867/j.issn.1001-8166.2009.07.0705. (in Chinese)
- 918 Williams, M., et al. (2009), Improving land surface models with FLUXNET data,
919 *Biogeosciences*, 6(7), 1341-1359, doi:10.5194/bg-6-1341-2009.

- Wilson, K., et al. (2002), Energy balance closure at FLUXNET sites, *Agricultural and Forest Meteorology*, 113(1-4), 223-243, doi:10.1016/S0168-1923(02)00109-0.
- Wohlfahrt, G., and P. Widmoser (2013), Can an energy balance model provide additional constraints on how to close the energy imbalance?, *Agricultural and Forest Meteorology*, 169, 85-91, doi:10.1016/j.agrformet.2012.10.006.
- Wyngaard, J. C. (1985), Structure of the planetary boundary-layer and implications for its modeling, *Journal of Climate and Applied Meteorology*, 24(11), 1131-1142, doi:10.1175/1520-0450(1985)024<1131:Sotpbl>2.0.Co;2.
- Xu, Z. W., Y. F. Ma, S. M. Liu, S. J. Shi, and J. M. Wang (2017), Assessment of the energy balance closure under advective conditions and its impact using remote sensing data, *Journal of Applied Meteorology and Climatology*, 56(1), 127-140, doi:10.1175/jamc-d-16-0096.1.
- Zhou, Y., D. Li, H. Liu, and X. Li (2018), Diurnal variations of the flux imbalance over homogeneous and heterogeneous landscapes, *Boundary-Layer Meteorology*, 168(3), 417-442, doi:10.1007/s10546-018-0358-2.
- Zhou, Y.Z., and Li, X., 2018. Progress in the energy closure of eddy covariance systems. *Advance in Earth Sciences*, 33(9), 898-913, doi:10.11867/j.issn.1001-8166.2018.09.0898. (in Chinese)
- Zhu, X., G. Ni, Z. Cong, T. Sun, and D. Li (2016), Impacts of surface heterogeneity on dry planetary boundary layers in an urban-rural setting, *Journal of Geophysical Research: Atmospheres*, 121(20), 12,164-112,179, doi:10.1002/2016JD024982.
- Zuo, H., X. Xiao, Q. Yang, L. Dong, J. Chen, and S. Wang (2012), On the atmospheric movement and the imbalance of observed and calculated energy in the surface layer, *Science China Earth Sciences*, 55(9), 1518-1532, doi:10.1007/s11430-012-4378-3.

Table 1. A summary of factors affecting the flux imbalance (I)

Factors	Qualitative relations to I	References
Averaging time (T)	The smaller T , the larger I	Finnigan et al. (2003); Charuchittipan et al. (2014); Kanda et al. (2004); Chen et al. (2006); Steinfeld et al. (2007); Schalkwijk et al. (2016); Zhou et al. (2018)
Height (z)	The larger z , the larger I	Kanda et al. (2004); Chen et al. (2006); Steinfeld et al. (2007); Huang et al. (2008); Schalkwijk et al. (2016); Zhou et al. (2018)
Horizontal mean velocity (U)	The smaller U , the larger I	Lee (1998); Stoy et al. (2013); Li et al. (2005); Franssen et al. (2010); Kanda et al. (2004); Chen et al. (2006); Steinfeld et al. (2007); Huang et al. (2008); Schalkwijk et al. (2016); Zhou et al. (2018)
The phase difference	The larger the phase difference between ground heat flux and net radiation, the larger I ; The larger the phase difference between vertical velocity and the scalar, the larger I	Gao et al. (2010); Gao et al. (2017)
Surface heterogeneity	The stronger surface heterogeneity, the larger I	Panin et al. (1998); Stoy et al. (2013); Xu et al. (2017); Zhou et al. (2018); Inagaki et al. (2006)
u_*/w_*	The smaller u_*/w_* , the larger I	Huang et al. (2008); Zhou et al. (2018)
z_i/L	The larger $-z_i/L$, the larger I	Schalkwijk et al. (2016)
z/L	The larger $-z/L$, the larger I	Franssen et al. (2010); McGloin et al. (2018)
Turbulent intensity	The smaller turbulent intensity, the larger I ; the smaller turbulent kinetic energy, the larger I	Zuo et al. (2012); Zhou et al. (2018)

Table 2. Summary of the experiments along with spatially and temporally averaged ABL characteristics in case B and H with standard deviations. The z_i represents the boundary-layer height and the u_* and w_* indicate the friction velocity and convective velocity, respectively. HFX and w_e (i.e., $\Delta z_i/\Delta t$) are the surface heat flux (i.e., the “true flux” in our study) and the mean entrainment rates, respectively.

Case Name	Heterogeneity scales (m)	z_i (m)	u_* (m/s)	w_* (m/s)	HFX (W/m^2)	w_e/w_*
B2000	2000	1415±157	0.30±0.22	2.52±1.56	457±869	0.018
B1200	1200	1388±142	0.29±0.22	2.50±1.55	460±890	0.017
B550	550	1306±147	0.33±0.22	2.55±1.54	463±913	0.013
B240	240	1287±135	0.37±0.21	2.52±1.51	487±937	0.012
H2000	2000	1444±189	0.34±0.22	3.05±1.51	512±795	0.016
H1200	1200	1436±178	0.34±0.21	3.08±1.50	515±811	0.015
H550	550	1384±172	0.37±0.22	2.99±1.52	520±828	0.014
H240	240	1379±160	0.39±0.22	2.92±1.53	521±848	0.014

953 **Table 3.** The slopes (K), intercepts (C) and coefficients of determination (R^2) between the f_2 and $l_w/(uT)$ (Fig.
 954 8) and $-z_i/L \times l_w/(uT)$ (Fig. 10).

case		$l_w/(UT)$	$l_w/(wsT)$	$l_w/(usT)$	$l_w/(eT)$	$-z_i/L \times l_w/(UT)$	$-z_i/L \times l_w/(wsT)$	$-z_i/L \times l_w/(usT)$	$-z_i/L \times l_w/(\bar{e}T)$
B	K	-19.26	-12.11	-5.47	-22.27	-0.06	-0.16	-0.02	-0.07
	C	1.11	0.83	1.21	1.17	0.96	1.09	1.02	1.03
	R^2	0.78	0.17	0.69	0.62	0.95	0.95	0.97	0.96
H	K	-15.23	-3.89	-3.26	-13.25	-0.05	-0.12	-0.01	-0.05
	C	1.00	0.75	1.00	0.99	0.94	1.03	0.98	0.98
	R^2	0.65	0.08	0.53	0.50	0.93	0.92	0.94	0.94
B + H	K	-16.86	-10.64	-4.54	-18.66	-0.05	-0.14	-0.01	-0.06
	C	1.04	0.82	1.12	1.10	0.95	1.06	0.99	0.98
	R^2	0.74	0.19	0.64	0.58	0.92	0.90	0.89	0.87

955

Figure 1. A conceptual model for flux imbalance from the cospectral perspective. The blue curve is the cospectrum calculated based on the LES results of B2000 (see Sect. 3.2) and the black curve is the fitted cospectrum based on Eq. (9) with $k_p=0.007$, $m=0.18$ and $\mu=5.5$. The k is the wavenumber and $F_{w\theta}$ is the cospectrum between w and θ . I is the flux imbalance. The k_p and k_{ec} are the peak wavenumber and critical wavenumber for EC, respectively.

Figure 2. Spatial patterns of surface temperature in B cases (a to d) and H cases (e to h).

Figure 3. The cross-sections (x - y) of temporally averaged vertical velocity during the final running hour in B cases and H cases at $z = 45$ m.

Figure 4. The cross-sections (x - z) of temporally averaged vertical velocity during the final running hour in H cases at $y = 3.5$ km.

Figure 5. The vertical profiles of ABL statistics: (a) potential temperature (θ), (b) variance of horizontal velocity (σ_u^2), (c) variance of vertical velocity (σ_w^2), and (d) TKE. All data are averaged in the final hour of simulation and (b, c, d) are normalized by the convective velocity. The boundary-layer height (z_i) is defined as the height where the minimum (negative) value of heat flux is found, and the vertical scale is normalized by z_i in each case.

Figure 6. (a) The vertical profiles of flux imbalance magnitude in different cases; and (b) the flux imbalance magnitude at 112 m as a function of surface heterogeneity scales (L_p) normalized by the boundary layer height (z_i).

Figure 7. The vertical profiles of f_1 with (a) the subgrid-scale heat flux included and (b) the subgrid-scale heat flux excluded. The black dash line is the fitted line (see Eq. 13).

Figure 8. The relations between f_2 and (a) $l_w/(UT)$, (b) $l_w/(w*T)$, (c) $l_w/(u*T)$, and (d) $l_w/(\overline{\epsilon}T)$. Only results in the range of $0.03 < z/z_i < 0.1$ are shown.

Figure 9. The f_2 as a function of $-z_i/L$. The marker indicates the mean of results in the range of $0.03 < z/z_i < 0.1$ and the bar indicates the range.

Figure 10. The relations between f_2 and (a) $-z_i/L \times l_w/(UT)$, (b) $-z_i/L \times l_w/(w*T)$, (c) $-z_i/L \times l_w/(u*T)$, and (d) $-z_i/L \times l_w/(\overline{\epsilon}T)$. Only results in the range of $0.03 < z/z_i < 0.1$ are shown.

Figure 11. The relations between f_2 and (a) $-z_i/L \times l_\theta/(UT)$, (b) $-z_i/L \times l_\theta/(w*T)$, (c) $-z_i/L \times l_\theta/(u*T)$, and (d) $-z_i/L \times l_\theta/(\overline{\epsilon}T)$. Only results in the range of $0.03 < z/z_i < 0.1$ are shown.

Figure 12. The (a) $-z_i/L$ and (b) $l_w/(UT)$ as a function of L_p/z_i . The marker in (b) indicates the mean of results in the range of $0.03 < z/z_i < 0.1$ and the bar in (b) indicates the range.

Figure C1. The spatial patterns of momentum roughness lengths in B cases (a to d) and H cases (e to h).

Figure D1. The vertical profiles of ABL statistics: (a) potential temperature (θ), (b) variance of horizontal velocity (σ_u^2), (c) variance of vertical velocity (σ_w^2), and (d) TKE. All data are averaged in the final hour of simulation and (b, c, d) are normalized by the convective velocity.

991 The boundary-layer height (z_i) is defined as the height where the minimum (negative) value of
992 heat flux is found, and the vertical scale is normalized by z_i in D cases.

993 **Figure D2.** The vertical profiles of flux imbalance magnitude in D cases; and (b) the flux
994 imbalance magnitude at 112 m as a function of surface heterogeneity scales (L_p) normalized by
995 the boundary layer height (z_i) in D cases.

Figure 1.

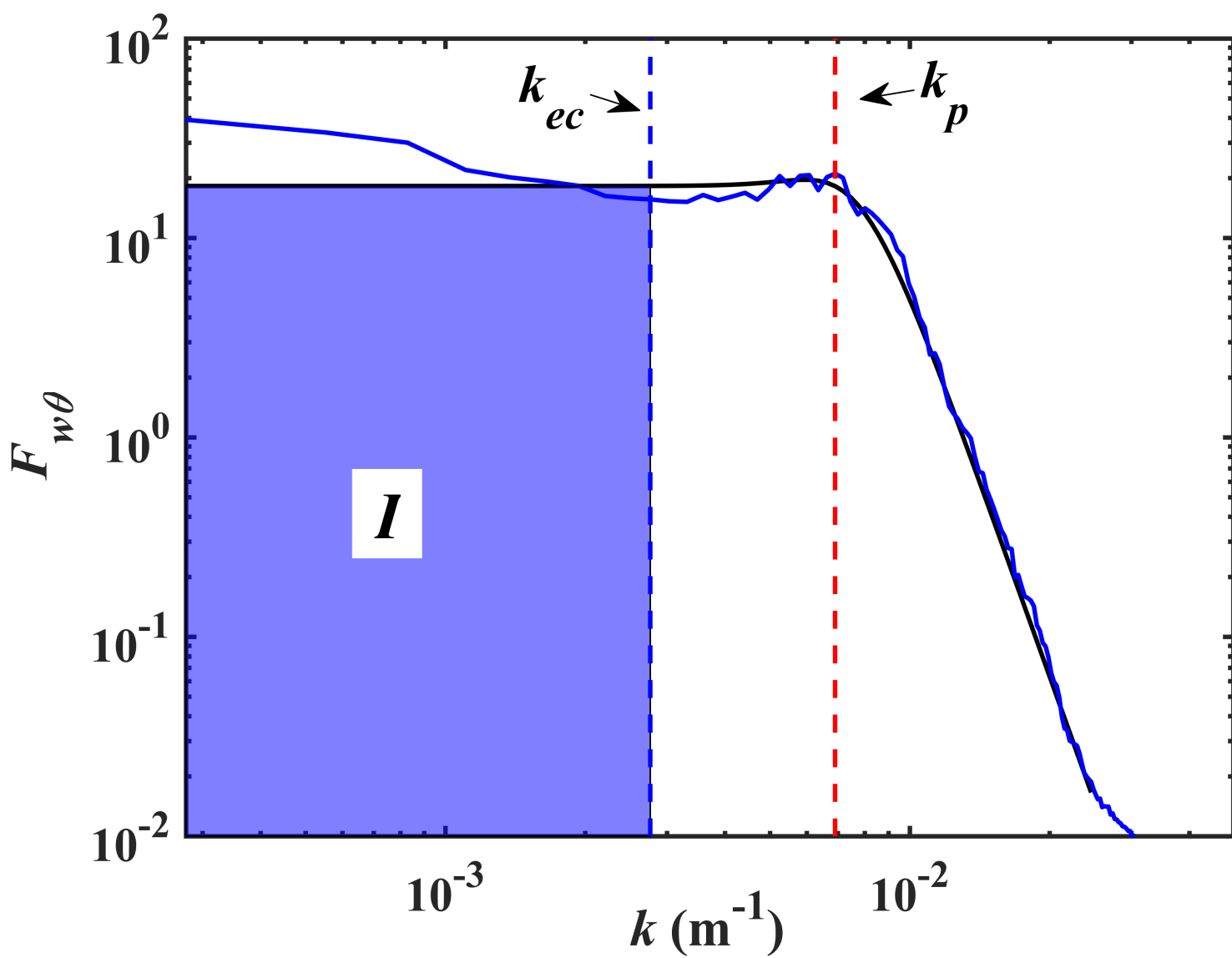


Figure 2.

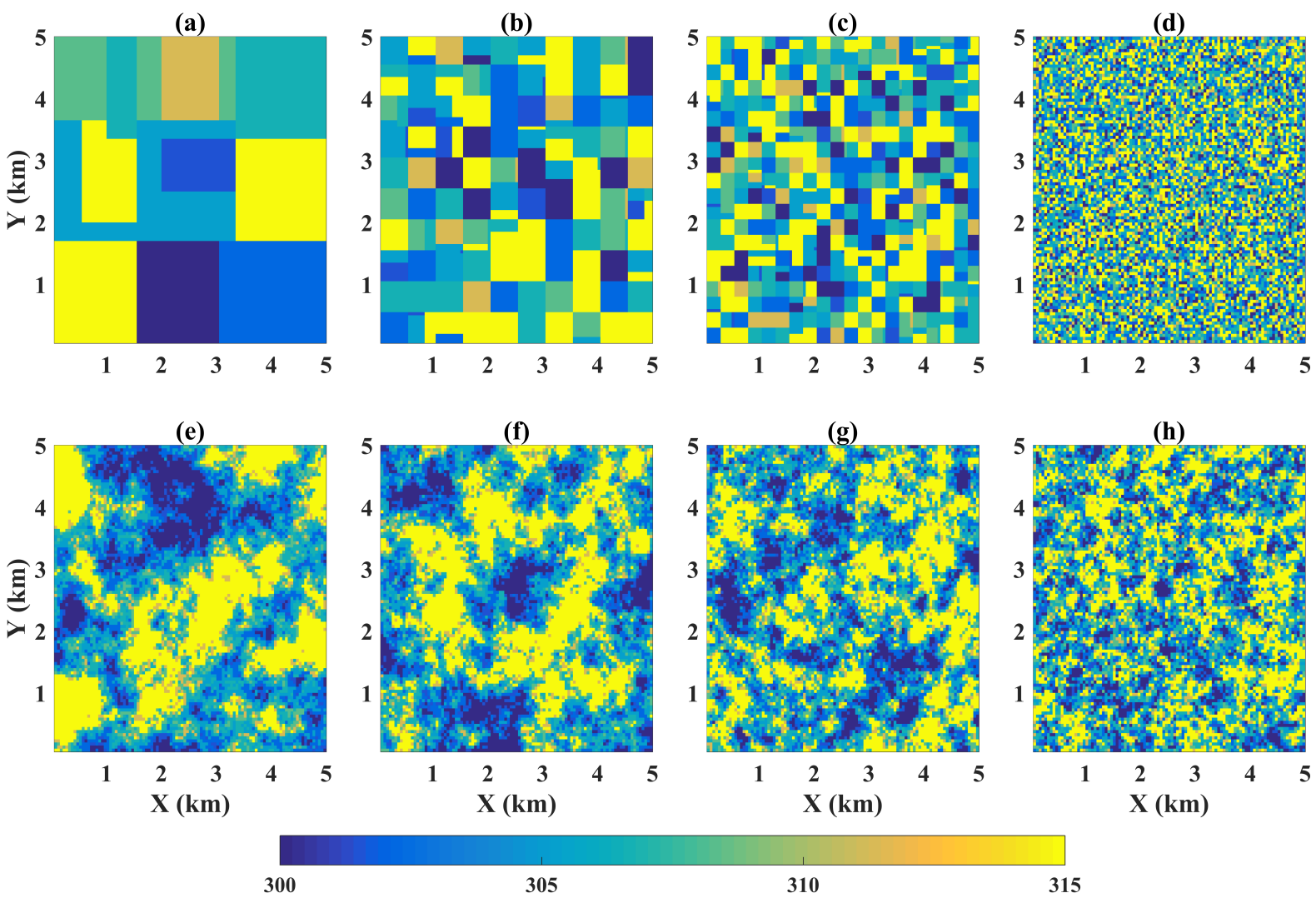


Figure 3.

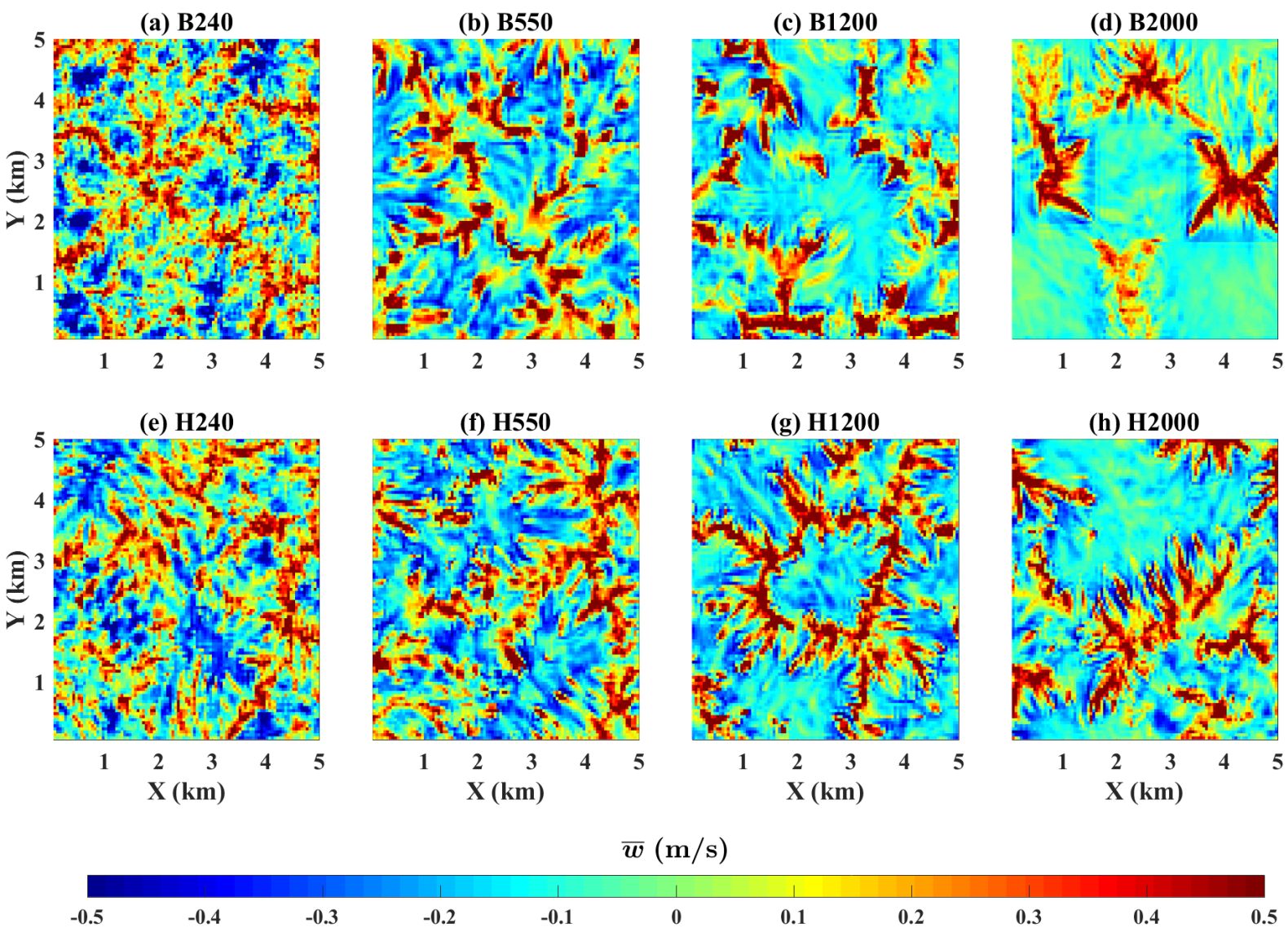


Figure 4.

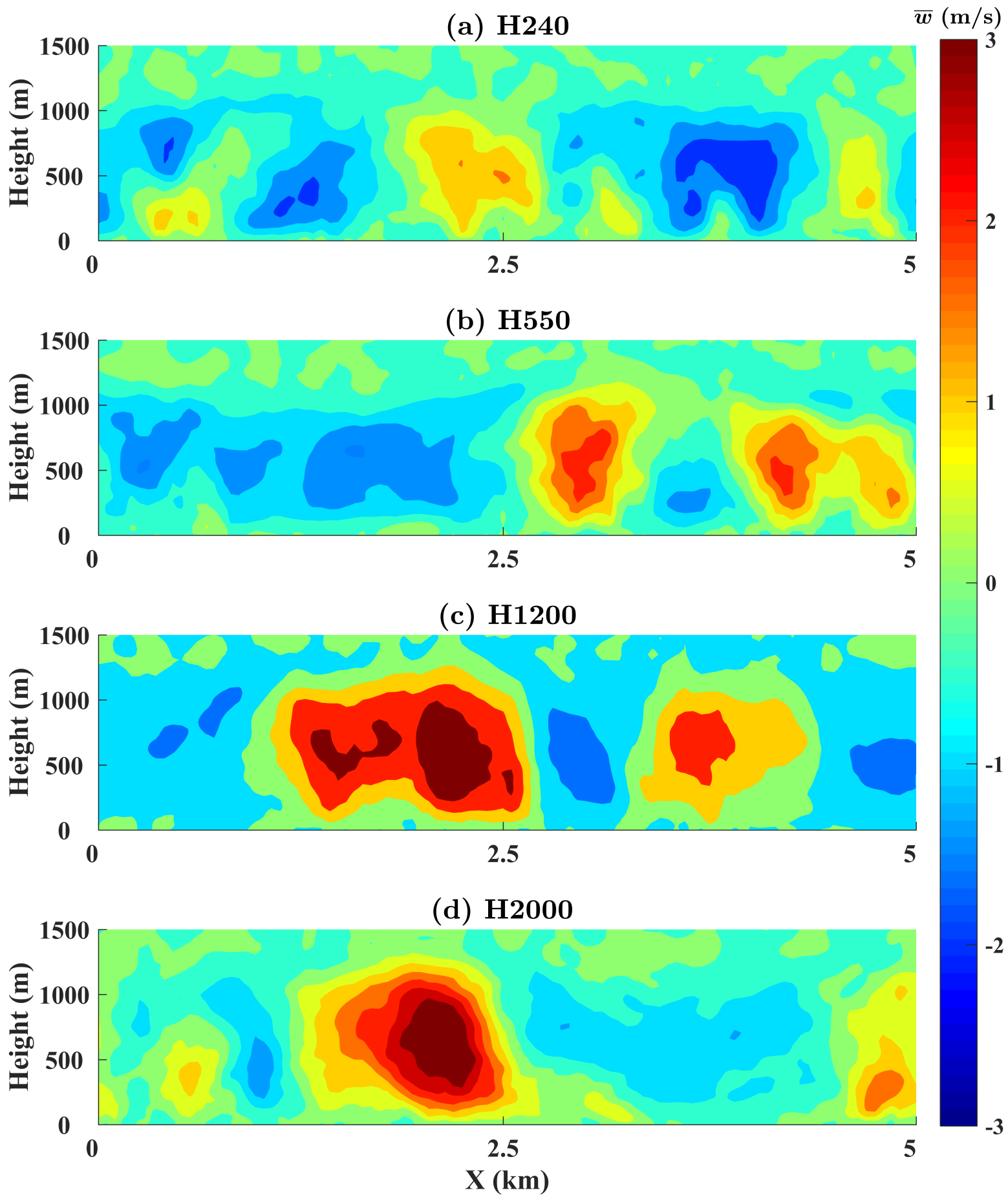


Figure 5.

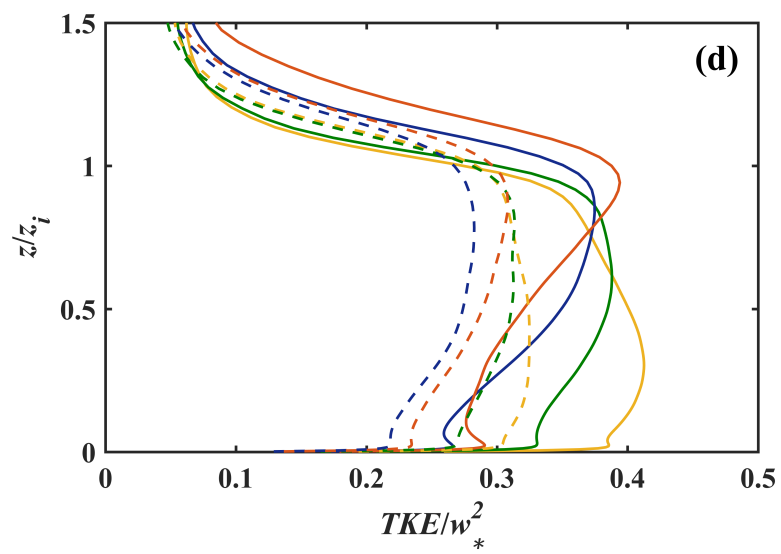
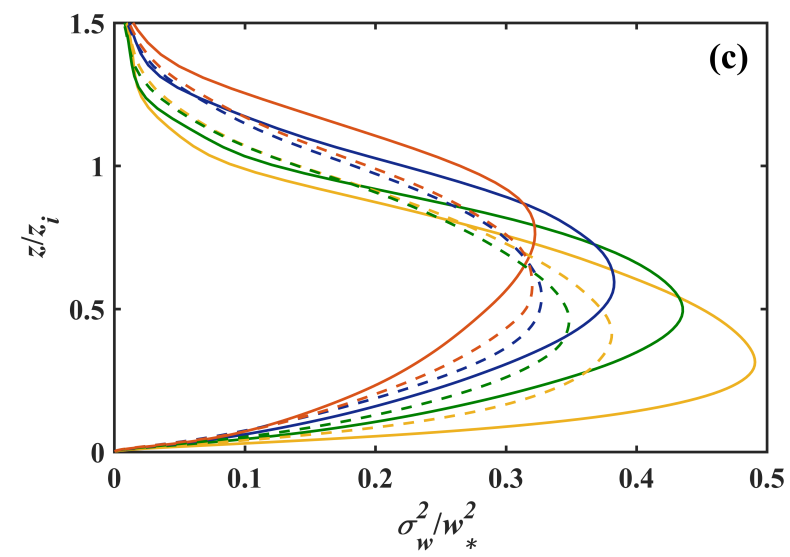
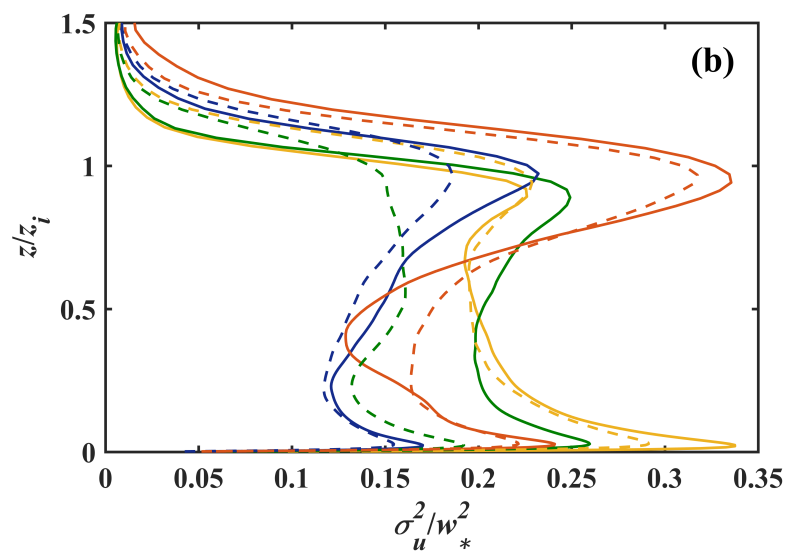
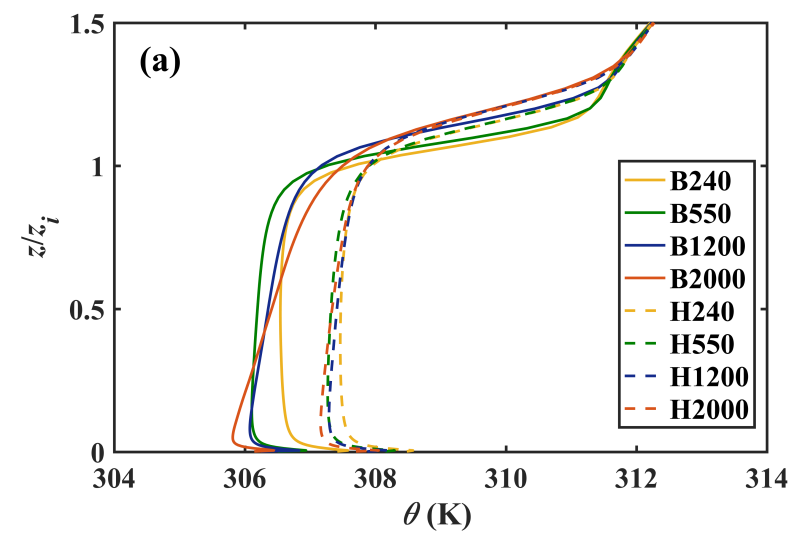


Figure 6.

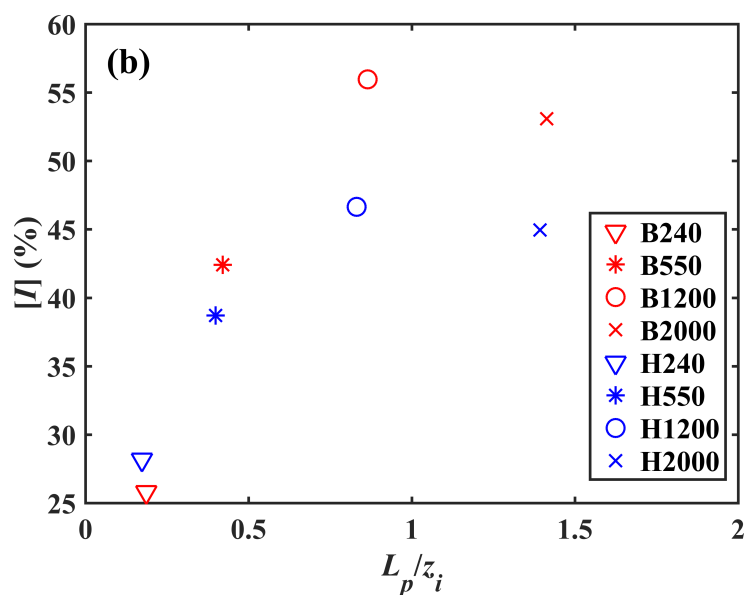
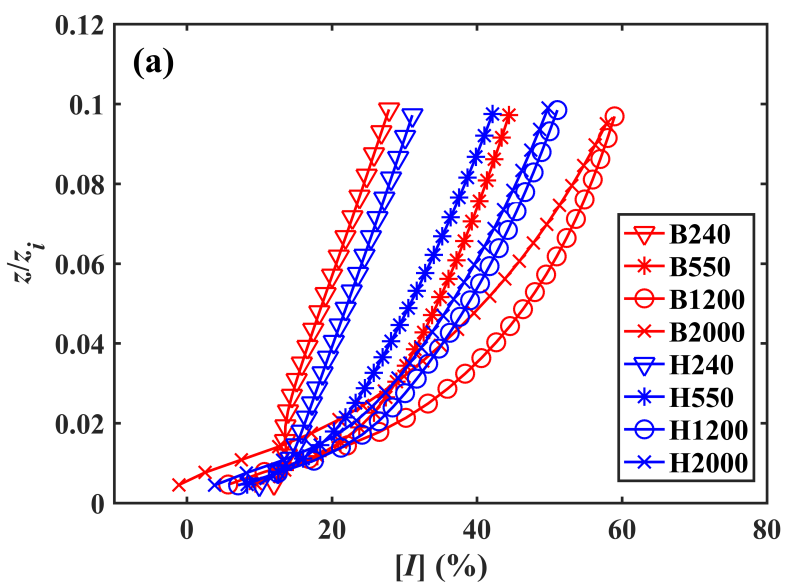


Figure 7.

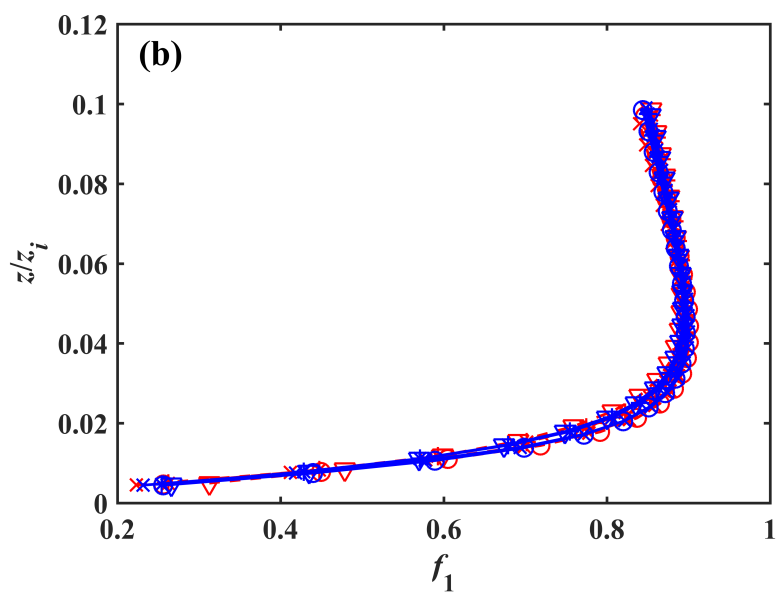
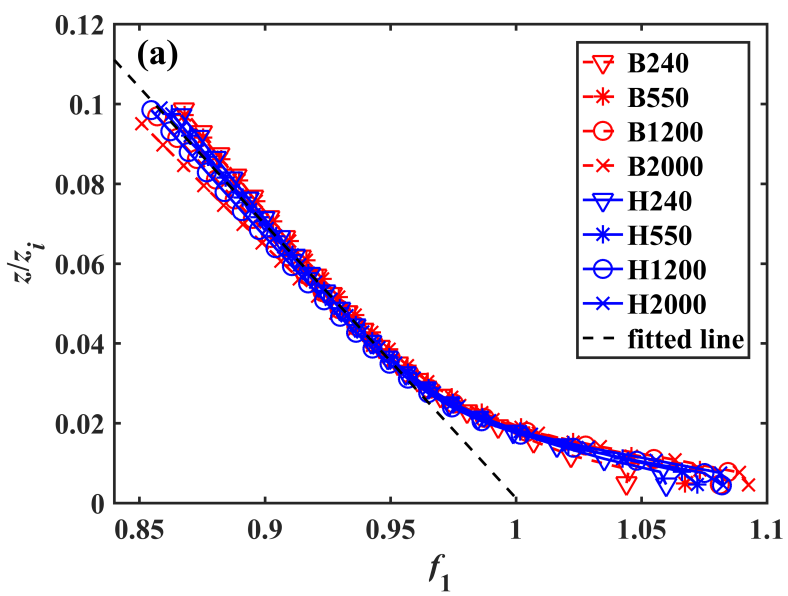


Figure 8.

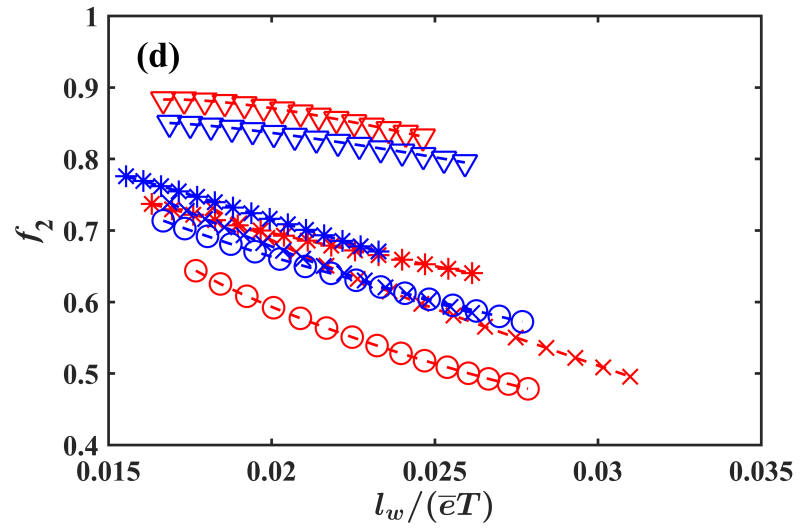
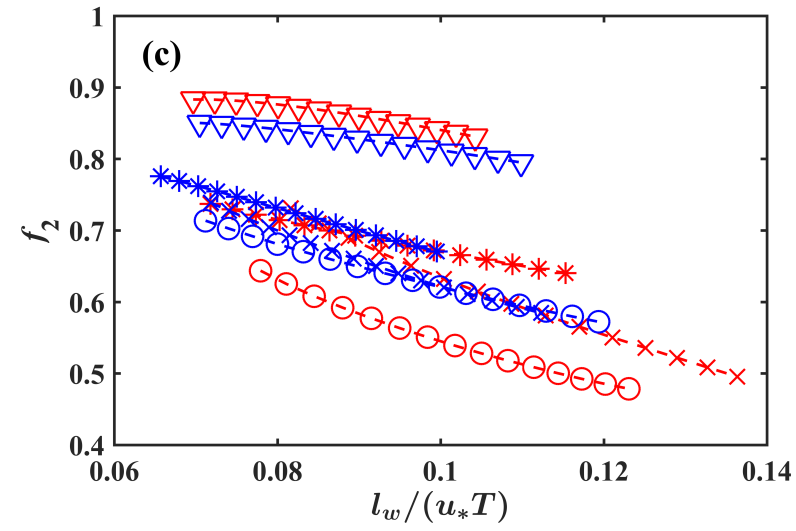
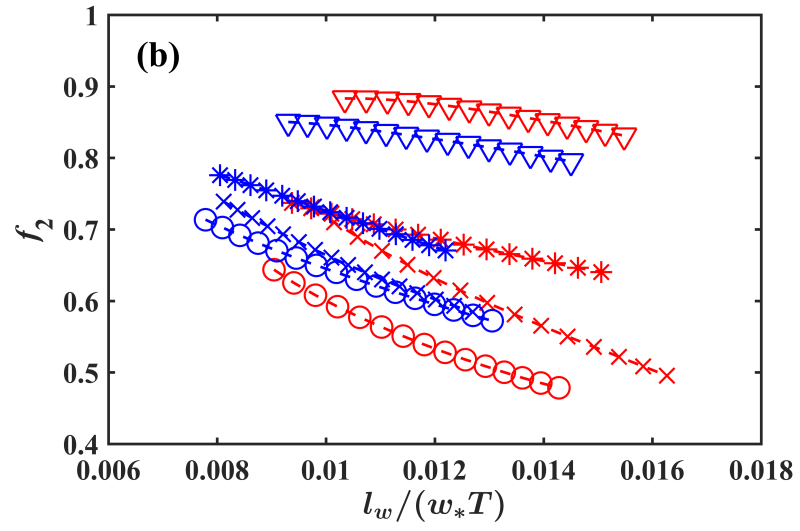
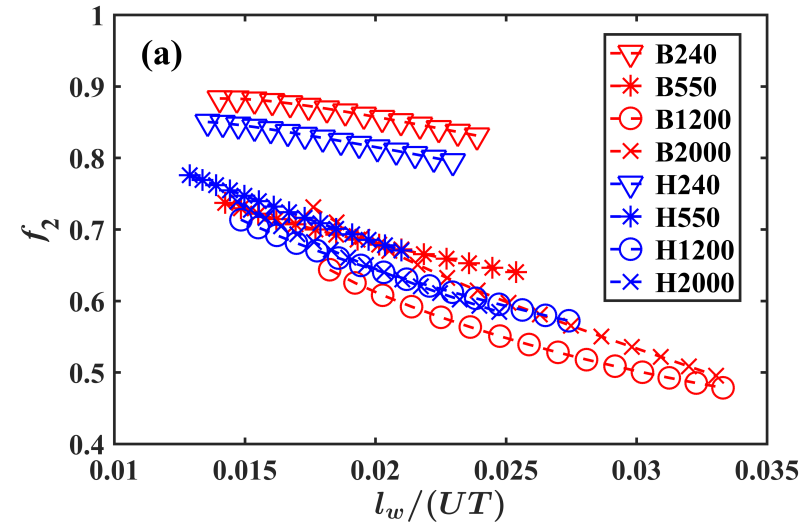


Figure 9.

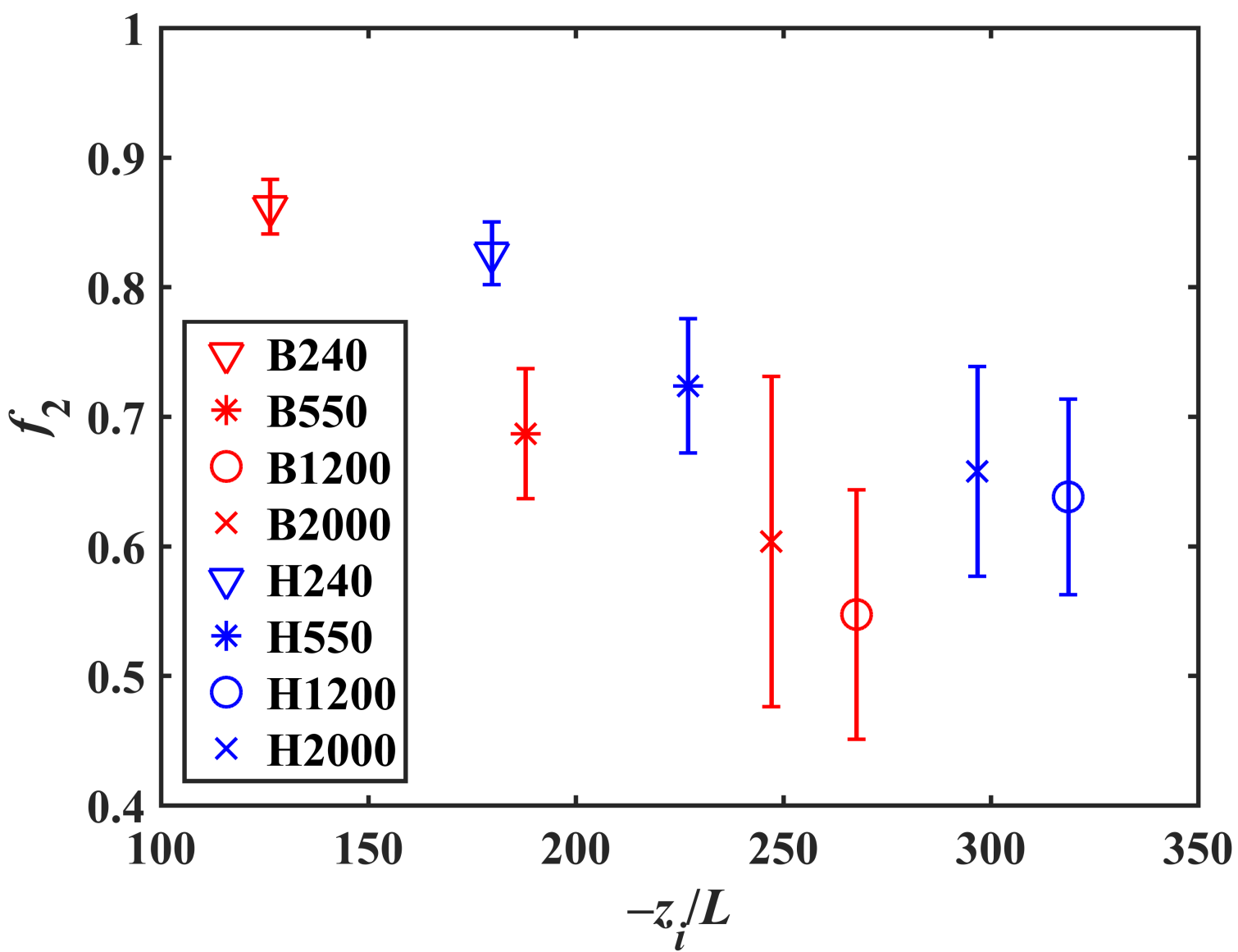


Figure 10.

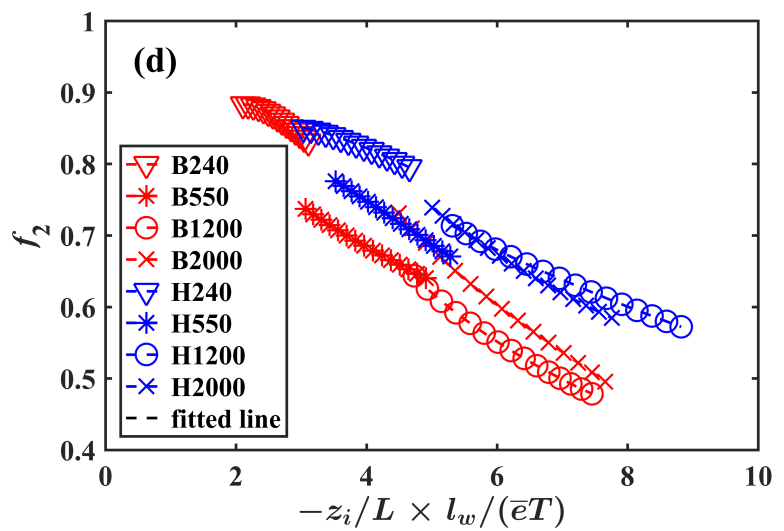
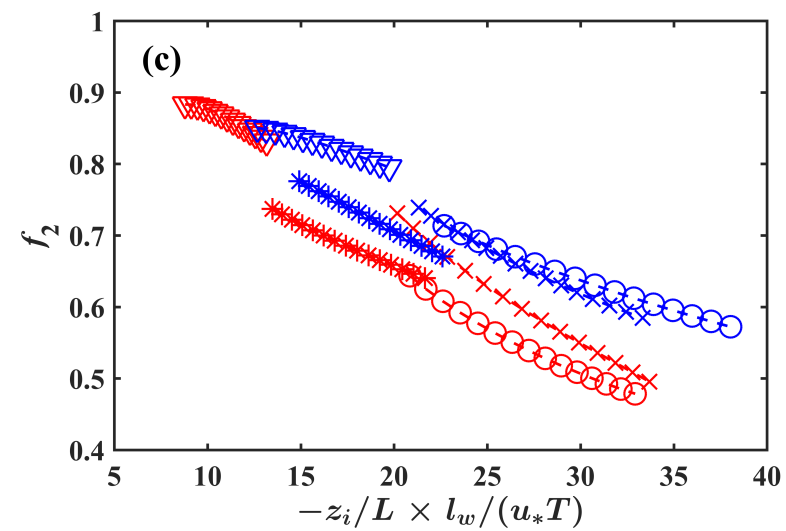
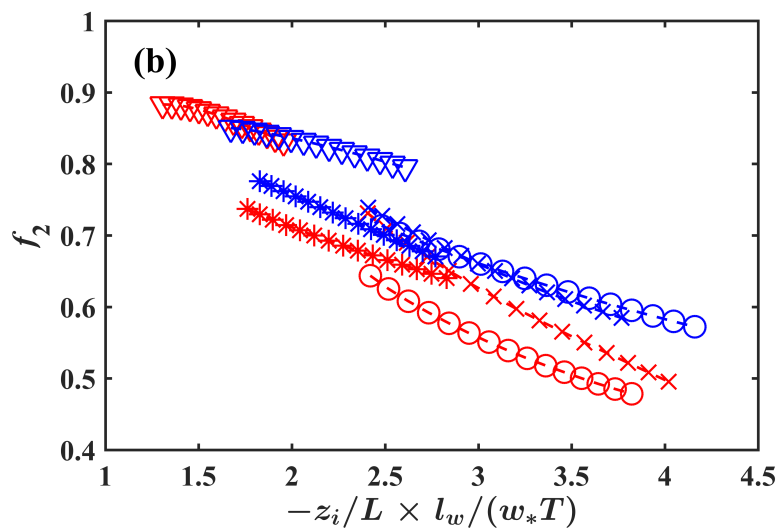
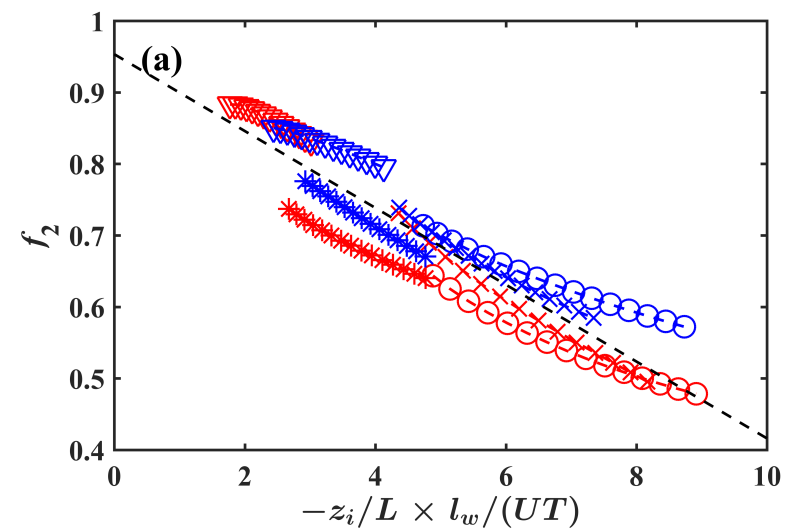


Figure 11.

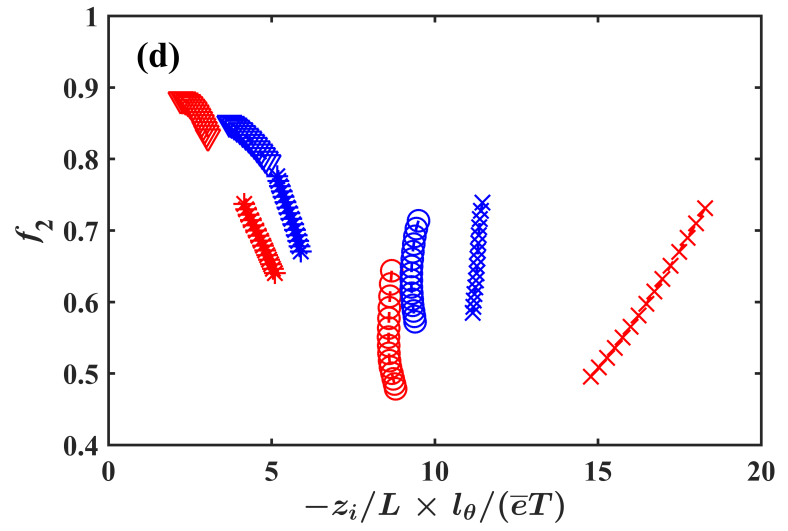
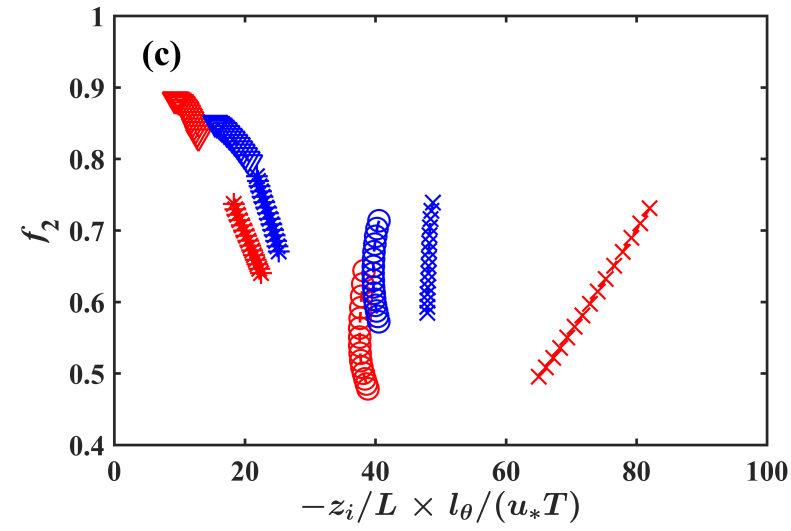
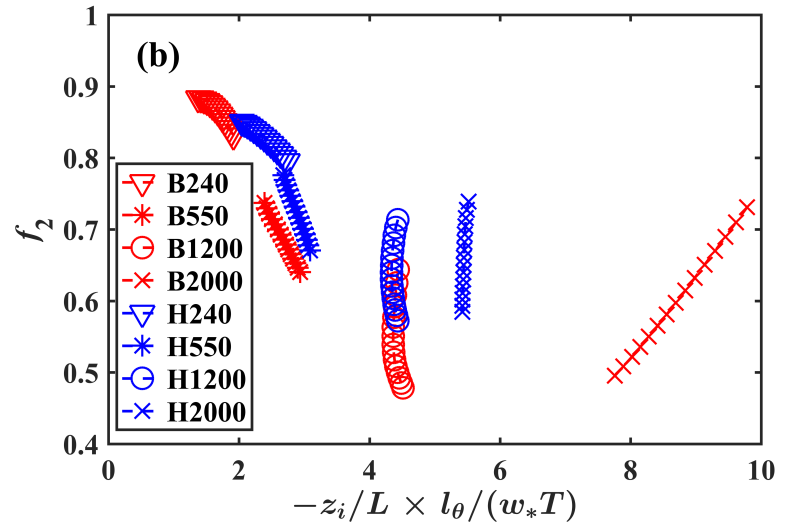
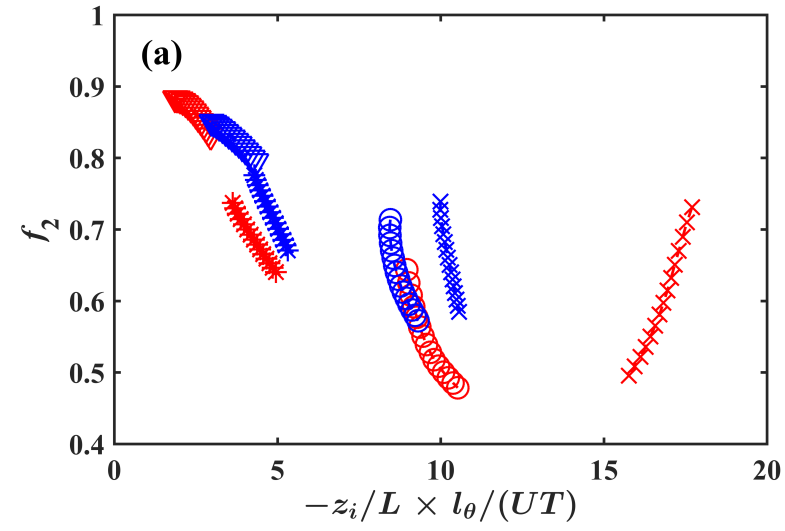


Figure 12.

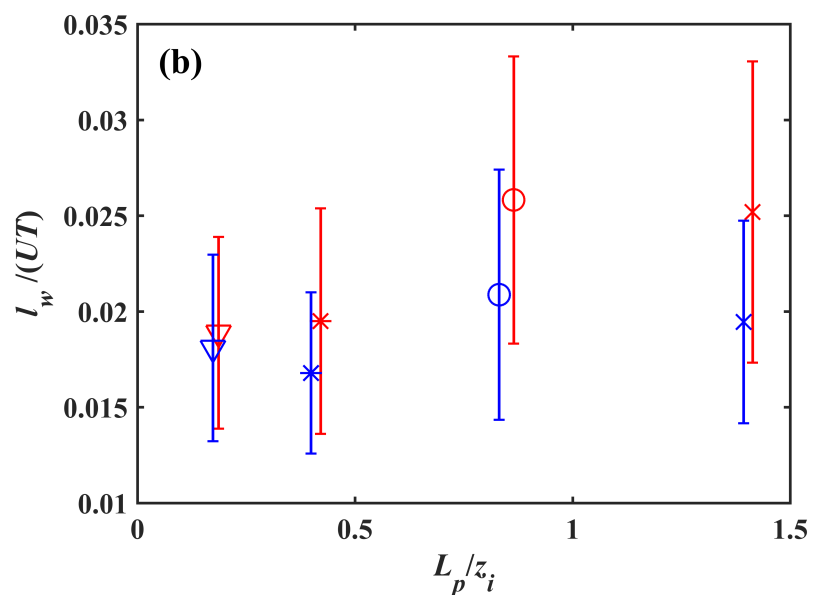
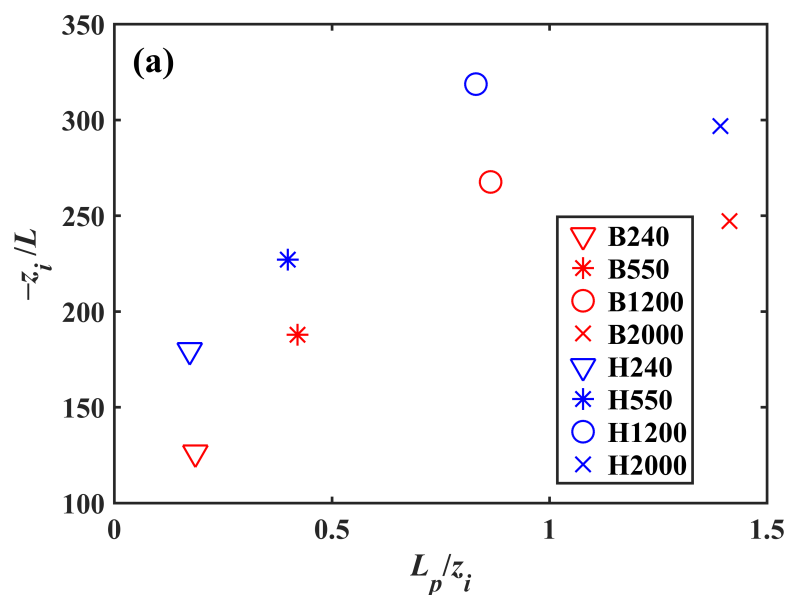


Figure C1.

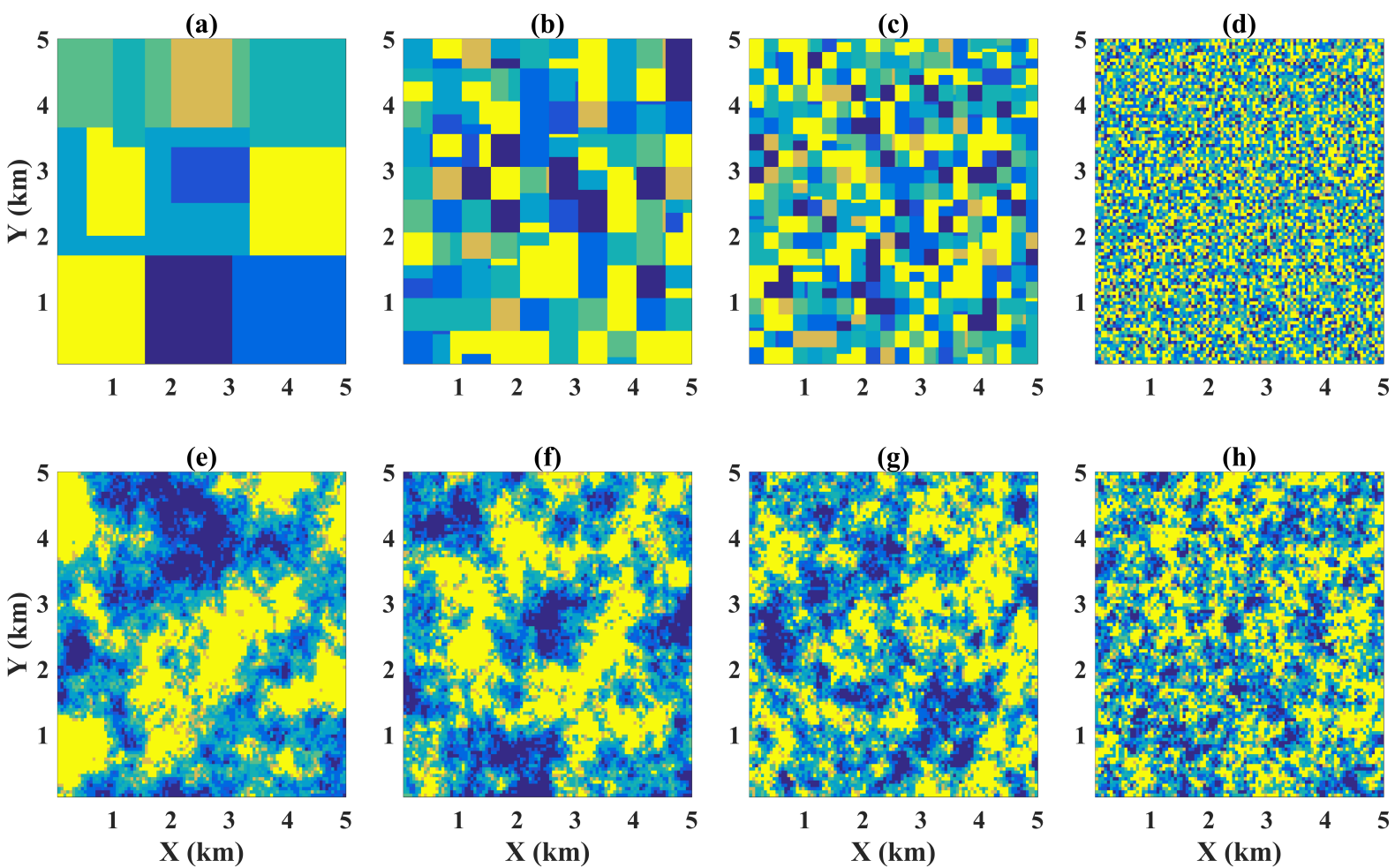


Figure D1.

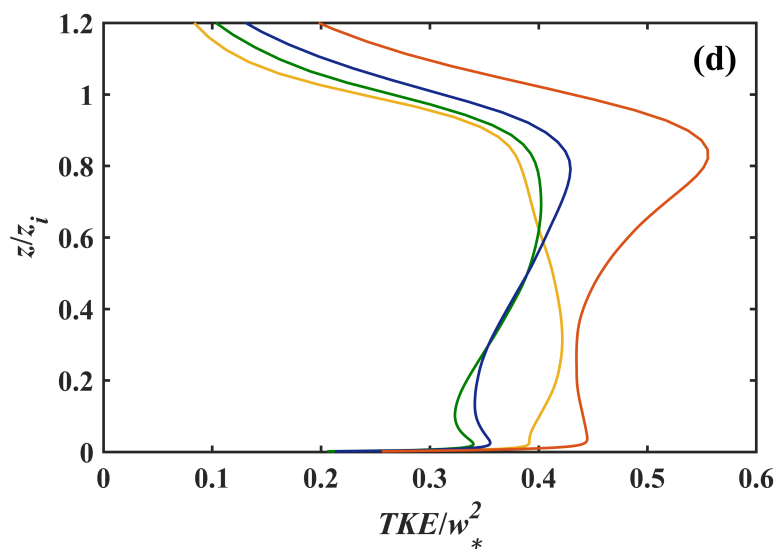
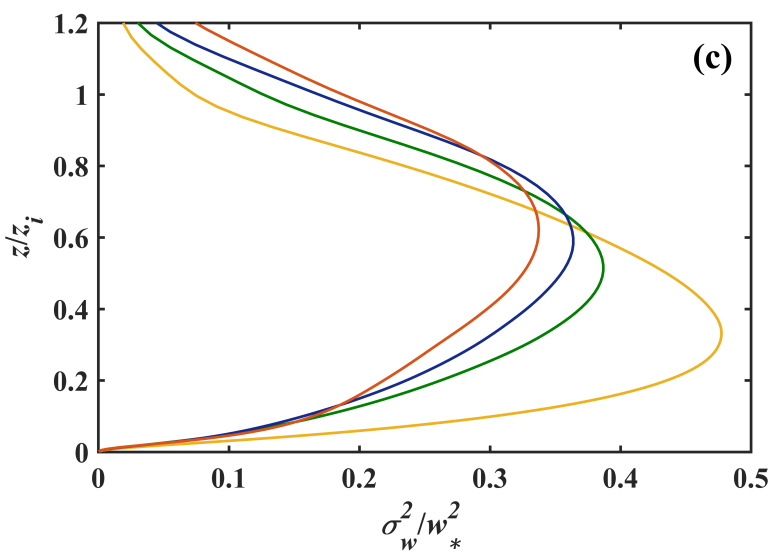
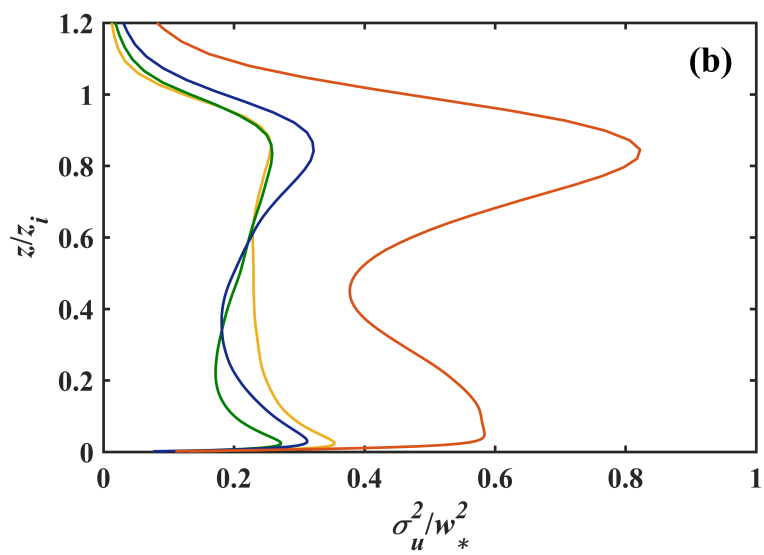
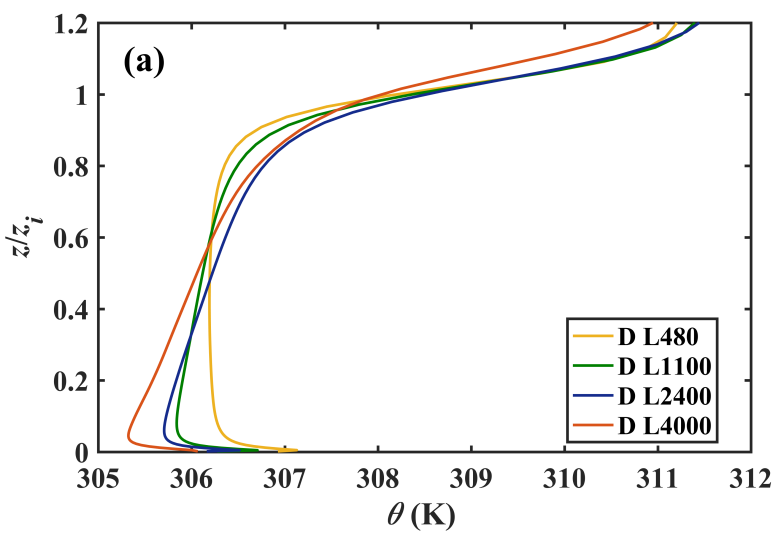


Figure D2.

